HHS Public Access

Author manuscript

Cell Rep. Author manuscript; available in PMC 2020 July 31.

Published in final edited form as:

Cell Rep. 2020 May 19; 31(7): 107648. doi:10.1016/j.celrep.2020.107648.

Distinct Transcriptomic Cell Types and Neural Circuits of the Subiculum and Prosubiculum along the Dorsal-Ventral Axis

Song-Lin Ding[1,2,*], **Zizhen Yao**[1], **Karla E. Hirokawa**[1], **Thuc Nghi Nguyen**[1], **Lucas T. Graybuck**[1], **Olivia Fong**[1], **Phillip Bohn**[1], **Kiet Ngo**[1], **Kimberly A. Smith**[1], **Christof Koch**[1], **John W. Phillips**[1], **Ed S. Lein**[1], **Julie A. Harris**[1], **Bosiljka Tasic**[1], **Hongkui Zeng**[1]

[1]Allen Institute for Brain Science, Seattle, WA 98109, USA

[2]Lead Contact

SUMMARY

Subicular regions play important roles in spatial processing and many cognitive functions, and these are mainly attributed to the subiculum (Sub) rather than the prosubiculum (PS). Using single-cell RNA sequencing, we identify 27 transcriptomic cell types residing in sub-domains of the Sub and PS. Based on *in situ* expression of reliable transcriptomic markers, the precise boundaries of the Sub and PS are consistently defined along the dorsoventral axis. Using these borders to evaluate Cre-line specificity and tracer injections, we find bona fide Sub projections topographically to structures important for spatial processing and navigation. In contrast, the PS sends its outputs to widespread brain regions crucial for motivation, emotion, reward, stress, anxiety, and fear. The Sub and PS, respectively, dominate dorsal and ventral subicular regions and receive different afferents. These results reveal two molecularly and anatomically distinct circuits centered in the Sub and PS, respectively, providing a consistent explanation for historical data and a clearer foundation for future studies.

Graphical Abstract

[*]Correspondence: songd@alleninstitute.org.

AUTHOR CONTRIBUTIONS

Conceptualization, S.-L.D. and H.Z.; Transcriptomic Data Acquisition, K.A.S., T.N.N., and B.T.; Connectivity Data Acquisition, K.E.H., P.B., K.N., and J.A.H.; Data Evaluation, Z.Y. and S.-L.D.; Clustering Analysis, Z.Y., L.T.G., and O.F.; Anatomical Mapping of Transcriptomic Clusters, S.-L.D.; Connectivity Data Analysis, S.-L.D.; Figure Preparation, S.-L.D.; Manuscript Preparation, S.-L.D., Z.Y., and H.Z., with input from other authors; Supervision, H.Z., B.T., J.A.H., E.S.L., J.W.P., C.K., and K.A.S. All authors read and commented on the manuscript.

SUPPLEMENTAL INFORMATION

Supplemental Information can be found online at https://doi.org/10.1016/j.celrep.2020.107648.

DECLARATION OF INTERESTS

The authors declare no competing interests.

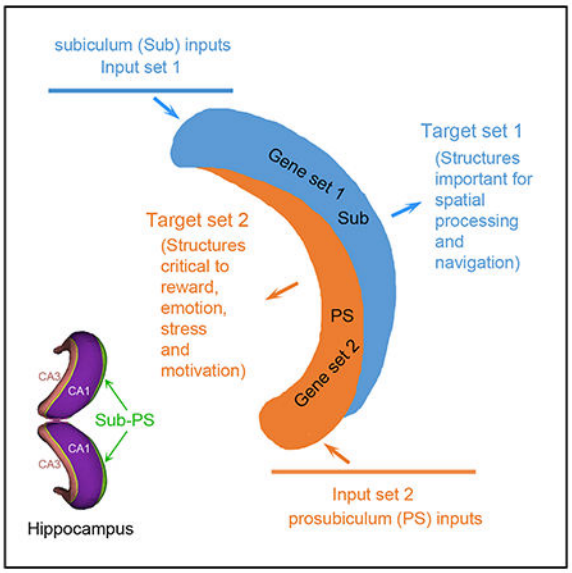

In Brief

Ding et al. show that the mouse subiculum and prosubiculum are two distinct regions with differential transcriptomic cell types, neural circuits, and dorsoventral extent. The former has obvious topographic projections to its main targets, while the latter exhibits widespread projections to many subcortical regions associated with reward, emotion, stress, and motivation.

INTRODUCTION

The subicular complex of the hippocampal formation (HF) has been reported to play important roles in many brain functions such as learning and memory, spatial navigation, emotion, reward, stress, motivation, and endocrine regulation (Aggleton and Christiansen, 2015; Herman and Mueller, 2006; O'Mara et al., 2009). This complex is also heavily involved in many neurological and psychiatric diseases such as Alzheimer's disease, temporal lobe epilepsy, schizophrenia, autism, anxiety disorder, and drug addiction (Coras et al., 2014; Godsil et al., 2013; Van Hoesen and Hyman, 1990). To explore the anatomical substrates of these functions and diseases, scientists have started to pinpoint specific subicular subfields for their cell types, neural circuits, physiological properties, and effects of lesion or stimulation (Bienkowski et al., 2018; Cembrowski et al., 2018a; Huang et al., 2017; Preston-Ferrer et al., 2016; Tang et al., 2016). An important first step to characterize the subicular subfields is to accurately identify and target these subfields and their cell types.

The subicular subfields mainly include the prosubiculum (PS), subiculum proper (Sub), presubiculum (PrS, including postsubiculum [PoS], i.e., dorsal PrS [PrSd]), and parasubiculum (PaS) (Ding 2013; Rosene and van Hoesen, 1987). The concept of the PS was proposed and refined by many scientists (Lorente De No, 1934; Saunders and Rosene, 1988; Saunders et al., 1988). Many previous studies in monkey have adopted the definition of the PS, which is a narrow and oblique region between CA1 and the Sub with strong acetylcholinesterase (AChE) staining (Arikuni et al., 1994; Barbas and Blatt, 1995; Fudge et

al., 2012; Saunders et al., 1988; Wang and Barbas, 2018; Yukie, 2000). However, the PS has not been well defined yet in rodent, in which the PS was often treated as part of the Sub with a dropout of the term PS (Ding, 2013). Accordingly, inconsistent and even opposite results often exist in PS and Sub studies between monkey and rodent and across different research groups. For example, in some retrograde tracing studies, neurons in the PS rather than the Sub were shown to project to the bed nucleus of stria terminalis (BST) and amygdala when the term PS was used in rat (Christensen and Frederickson, 1998; Howell et al., 1991) and monkey (Fudge et al., 2012; Rosene and van Hoesen, 1987; Saunders et al., 1988; Wang and Barbas, 2018). In contrast, when the term PS was not used, neurons in the Sub were reported to project to the BST and amygdala in other studies of the rat (Kishi et al., 2006; Ottersen, 1982; Shi and Cassell, 1999; Veening, 1978; Weller and Smith, 1982). A similar situation was observed for projections from the PS and the Sub to the ventromedial prefrontal cortex (PFvm, including prelimbic cortex [PL] and infralimbic cortex [IL]) and ventral striatum (VS, including nucleus accumbens [ACB] and olfactory tubercle [OT]). For instance, after retrograde tracer injections into the IL or VS, labeled neurons were mostly found in the PS (Jay et al., 1989) or in the “proximal Sub” (close to CA1; roughly corresponding to the PS) rather than in the “distal Sub” (close to the PrSd) of the rat (Christie et al., 1987; Ishizuka, 2001; Phillipson and Griffiths, 1985; Witter, 2006; Witter et al., 1990). All the above findings suggest the existence of the PS as a distinct entity from the Sub, with distinct outputs. If it is confirmed that the PS rather than the Sub projects to the amygdala, VS, BST, and IL—structures heavily involved in emotion, reward, stress, and motivation (Aggleton and Christiansen, 2015; Herman and Mueller, 2006; O’Mara et al., 2009; Strange et al., 2014)—then it is reasonable to hypothesize that it is the PS rather than the Sub that plays important roles in these brain functions and related diseases. Clarification of this issue will lead to a clearer picture of region- and cell-type-specific circuits of the PS and Sub to facilitate more accurate functional studies.

In this study, we test and verify the hypothesis that the PS exists as a distinct region and has distinct cell types and neural circuits in mice. We use unbiased hierarchical clustering of scRNA-seq (single-cell RNA sequencing) transcriptomic profiles to identify cell types, showing that distinct molecular cell types exist in the Sub and PS. Using region-specific gene markers, we consistently delineate and update the boundaries of the Sub and the PS along the dorsal-ventral (DV) axis. With these boundaries as a guide, we reveal differential afferent and efferent connections of the Sub and PS at the whole-brain level. Utilizing different Cre lines, we trace brain-wide projections of major cell types in the Sub and PS. Together, we have systematically linked distinct cell types, molecular signatures, connectivity, and anatomy of the Sub and PS and opened the potential to specifically target cell types and related circuits in future studies to understand related functions and diseases.

RESULTS

Transcriptomic Taxonomy of Glutamatergic Neurons in the Sub and PS

Since recent molecular and connectional studies had not reached a consensus regarding cell types and connectivity patterns of the mouse subicular regions (Bienkowski et al., 2018; Cembrowski et al., 2018a, 2018b), we first performed a transcriptomic survey of 17,062

glutamatergic cells isolated from the subicular complex (STAR Methods). In addition, the rodent homolog of the monkey and human hippocampo-amygdaloid transition area (HA) is also located in this region, mainly ventral to the PS (Allen Mouse Brain Common Coordinate Framework, CCFv3; https://atlas.brain-map.org, Wang et al., 2020). We performed two small micro-dissections (including the regions PrS-PoS-PaS and Sub-PS-HA) and a larger one (including both regions) along the DV axis of the HF (Figure 1A). Cells from the first two dissections were sequenced with the SMART-seq v4 method (Tasic et al., 2018), which had a smaller sample size, while those from the larger dissection were sequenced with the 10X Chromium v2 method, which allows much larger sample sizes.

We performed a consensus clustering to combine the SMART-seq and 10X datasets. For this study, we calculated a dendrogram specifically for the glutamatergic class of neurons, which include 2,182 SMART-seq cells and 14,880 10X cells. For visualization, 10X cells were downsampled to up to 200 cells per cluster (original cluster, OC; Figure 1B). From this dendrogram, based on marker gene localization (Figure S1A; Table S1), we identified three major branches that correspond, respectively, to principal cells in (1) layers 2, 3, and 5 of PrS-PoS-PaS and adjoining retrosplenial (RS) and entorhinal cortex (EC) regions (OC2-OC22, but not OC23 and OC24); (2) the pyramidal cell layer of Sub-PS-HA and adjoining CA1 (OC23-OC38); and (3) the deepest layers of all related regions (OC39-OC50). OC1 (for dentate gyrus cells) and OC51 (for Cajal-Ritzius cells) are two outliers. OC2-OC22 of the first major branch (at the left of Figure 1B), together with OC1 and OC51, were excluded from further analysis because they do not contain cells from our focused Sub-PS-HA region in this study. OC23 and OC24 of the first branch were located in the most superficial pyramidal layer of PS (PSpy). The second major branch (OC25-OC38) was spatially localized to deep PSpy (OC25, OC26), the pyramidal layer of Sub (Spy; OC27-OC31), the superficial pyramidal layer of HA (HApy) and PSpy (OC32-OC35), and the pyramidal layer of adjoining CA1 (CA1py; OC36-OC38). The third major branch (OC39-OC50) was localized to the polymorphic layer of the Sub and PS (Spo and PSpo; OC39-OC41), layer 6 (L6) of all related regions (OC42-OC47), and layer 6b (L6b) of related regions (OC48-OC50). L6 and L6b were named because they are continuous with L6 and L6b of adjoining cortices and are separate from the overlaying polymorphic layer at the transcriptomic and anatomic levels (e.g., Figures 1B, 2S, 2T, and S1G).

To explore if more refined clusters could be revealed from the Sub-PS-HA region, we pooled all cells (n = 8,648) from OC23-OC38 and OC39-OC44 and performed hierarchical re-clustering (RC) as shown by the dendrogram and tSNE (t-distributed stochastic neighbor embedding) plot (Figures 1C and S2). This resulted in 25 clusters in the Sub-PS-HA region, three clusters in the adjoining CA1, and one cluster in the deep L6 of the PrS (Figures 1C, 1D, 2A–2T, and S1B–S1N). Note that L6b cells (OC48-OC50) and L6 cells from the medial and lateral EC (OC45 and OC46) and PrS-PoS (OC47, superficial L6) were not included in this RC. Compared with the OC, RC revealed a few more clusters/cell types in the PSpy and HApy but not in the Spy and adjoining CA1py (Table S1). Interestingly, in both clusterings, the PSpy is more similar to the CA1py and HApy than to the Spy by gene expression distance (Figures 1B and 1C). Generally, seven major subclasses can be identified in the Sub-PS-HA region (Figure 1C; Table S1): Spy (RC1-RC3), deep PSpy (RC6-RC8), superficial PSpy (RC10-RC14), HApy (RC17-RC19), most superficial PSpy (RC20-RC23),

Spo and PSpo (RC24-RC26), and L6 of the Sub and HA (RC28 and RC29). Cells from two small clusters (RC4 and RC5) lie in the PSpy at the border between the ventral Sub and PS. Therefore, taking away adjoining CA1 (RC9, RC15, and RC16) and PrSd (i.e., PoS; RC27) and adding L6b of the Sub and PS from the OC (OC48 and OC49), a total of 27 clusters or cell types were revealed in the Sub-PS-HA region. These cell types were partially covered in the overall Sub region sampled by Cembrowski et al. (2018b). The latter study revealed eight clusters, which mainly represent coarse subclasses, probably due to a smaller sample size used (n = 1,150 cells) (for comparison, see Table S1; Figure S2A).

Anatomical Mapping of Transcriptomic Clusters

To facilitate accurate targeting and manipulation of specific cell types, we tried to correlate transcriptomic clusters with anatomical locations. For this, we surveyed the Allen Brain Atlas (Lein et al., 2007) *in situ* hybridization (ISH) dataset using distinct gene markers revealed at different branch levels (Figures 1D and S1B; Table S1). As shown in Figures 1, 2, and 3, *Nts, Fn1, Rxfpl, Adcyapl, Gpr101*, and *Bcl6* are expressed in most neurons located in the anatomically defined Spy region, while genes such as *Ntng2* and *Syt17* are expressed in most neurons located in the PSpy. The HA region also displays region-enriched expression of genes such as *Col23a1, Rab3b, Id4, Abca8a, Gpc3, Unc5d, Lpl*, and *Car10* (e.g., Figures S1C–S1F). The HA region was previously treated as a part of ventral Sub or ventral CA1 in rodent (Bienkowski et al., 2018; Paxinos and Franklin, 2012) but has recently been found to be the homolog of monkey and human HA (CCFv3; Ding et al., 2016). The HA is characterized by densely packed pyramidal-like neurons in its superficial layer (HApy) and less densely packed small neurons in its deep layers (HAL6) (Figures S1C–S1F; Ding and Van Hoesen, 2015). The polymorphic layers of the Sub and PS (Spo and PSpo) show region-specific expression of *Ly6g6e, Cntn6, Pamr1, Cbln2*, and *St3gal1* (Figures 1D, 2M, 2N, and 2Q), while the deeper layer (L6) of the Sub and HA expresses another set of region-specific genes such as *Sema3e, Thsd7b*, and *Nppc* (Figures 2S and 2T; the PS appears to lack this layer or has only scattered cells). Finally, a layer of cells lined at the gray-white matter border (L6b) of the PrSd and Sub was also revealed (Figure S1G).

Three clusters (RC1-RC3) could be further identified in the Spy. RC1 and RC2 correspond to the distal Spy (away from the PS), while RC3 corresponds to the proximal Spy (close to the PS). The gene markers for RC1 cells include *Cntn6, Dio3, Npsr1, Angpt1, St8sia2*, and *Pdzrn4*, while those for RC2 include *Igfbp4, Cyp26b1, Scn4b*, and *Whrn* (Figures 1D, S1H, and S1I). Representative markers in RC3 include *Sntg2, S100b, Col6a1, Alk*, and *Glra3* (Figures 1D and S1J). RC4 is a small cluster with cells located in the superficial pyramidal layer of the ventral Sub bordering the PS and expresses *Teddm3, Luzp2, Galnt14, Fam19a1*, and *C1ql2* (Figure S1K). Another small cluster, RC5, has its cells at the superficial S-PSpy border and expresses *Eps8, Dcc, Gpr101, Cyp26b1*, *Whrn, Alk, Gpc5*, and *Glra3* (Figures S1L–S1N).

In contrast to the Spy, the PSpy contains many subtypes (12 clusters), representing highly heterogenous cell types that often show laminar organization (Figures 2 and S3). RC6-RC8 and RC10-RC14 represent the deep (PSpy-de) and superficial PSpy (PSpy-su2), respectively, while RC20-RC23 were mapped to the most superficial PSpy (PSpy-su1;

Figures 2G–2L and S3). *Cbln4* and *Nos1* are the representative markers for the PSpy-su1 (RC20-RC23; Figures S3B–S3F), which is generally located superficial to the PSpy-su2 (RC10-RC14). The latter expresses another set of genes such as *Dlk1* and *Col25a1* (Figures S3G–S3K and S3S–S3U). This is consistent with the non-overlapping expression of *Cbln4* and *Dlk1* reported by Cembrowski et al. (2018b). However, some genes *(Tgfb2* and *Satb2)* are expressed in both groups (Figures S3A and S3L-S3P). Moreover, gene expression difference along the DV axis is detected in the PSpy-de group (RC6-RC8). For example, *S100b* and *Slc17a6* tend to be expressed strongly in the dorsal portion (RC8; Figures 1D, 2G, and 2S), while *Syt10* and *Mgp* are expressed in the ventral portion (RC6 and RC7; Figure S3A). In the PSpy-su1 (RC20-RC23) and PSpy-su2 (RC10-RC14) subclasses, differential gene expression along the DV axis is also found (Table S1).

Genes predominantly expressed in the PSpo (RC24; e.g., *Cacng5*, *Htr2c*, *Trhr*, and *Gdpd2*) or Spo (RC25 and RC26; e.g., *Plcb4, Pirt, Abi3bp*, and *Pdzrn4)* are also observed, although more genes are expressed in both the PSpo and Spo (Figures 1D and 2M-2S). The latter genes include *Pamr1, Cbln2, Ly6g6e, Chrm2, Tle4, Kcnmb4, St3gal1*, *Trp53i11*, and *Drd1a* (Figures 2M, 2N, and 2Q). Finally, genes expressed in the L6 (RC28 and RC29) and L6b (OC48 and OC49) of the Sub, PS, and HA often extend to the adjoining PrS (RC27, OC50) and EC. L6 cells express genes such as *Sema3e, Thsd7b, Car10*, and *Nppc*, and HA has the thickest L6, which predominantly expresses *Sema3d, Foxp2, Thsd7b*, and *Car10* (Figures 1D, 2T, and S1F). L6b is just a single-cell layer at the gray-white matter border expressing *Nxph4, Cplx3*, and *Ctgf* (Figure S1G).

Precise Borders, Topography, and Extent of the Sub and PS

The borders of the Sub, PS, HA, and adjoining CA1 were not consistently defined previously in literature and brain atlases (e.g., Bienkowski etal., 2018; Cembrowski etal., 2018b; Paxinos and Franklin, 2012). Since we identified reliable and differential markers for these regions at the transcriptional level, we next delineated precise boundaries between these regions along their DV axis with a combined use of these gene markers in sequential coronal (Figure 3) and sagittal (Figure S4) sections. For convenient description, the Sub, PS, and CA1 are roughly subdivided into dorsal (d) and ventral (v) parts since no clear markers are available for the DV borders. In coronal sections, the DV border between the Sub and the PS was placed at the dorsal edge of the most caudal PS (for Sd and Sv; Figure 3K) or at the dorsal edge of the most caudal CA1 (for PSd and PSv; Figure 3H). The locations of theSd, PSd, CA1d, Sv, PSv, and CA1v, as well as their topography, are shown on sequential coronal sections stained for *Nts* (Figures 3A–3M) and *Ntng2* (Figures 3N–3R), which show complementary expression patterns. The Sd medially adjoins the granular part of the retrosplenial cortex (RSg) at dorsorostral levels (Figures 3A–3E) and the PrSd at ventrocaudal levels (Figures 3F–3K). Laterally, the Sd adjoins the PSd at rostrodorsal levels (Figures 3A–3H) and the PSv at caudoventral levels (Figures 3I–3K). The Sv adjoins the PrSv medially, the PSv rostrally, the LEC (lateral EC) laterally, and the MEC (medial EC) caudally (Figures 3K–3M). The PSd is located lateroventral to the Sd and mediodorsal to CA1d, while the PSv is located rostral to the Sv and ventral to CA1v. Both CA1v and the PSv are connected with the cortical amygdalar nucleus via the HA (Figures 3E–3H, S3A, and S3G–S4I). From dorsorostral to ventrocaudal levels, the width and extent of the Sub

decreases while that of the PS increases. Based on the present delineation, it is surprising to find that the previously defined Sv in fact belongs to the PSv (see the region marked with ** in Figures 3I, 3J, 3N, and 3O) because this region expresses many typical PS (e.g., PSd) genes, including *Ntng2, Calbl, Nnat, Syt17*, and *Adrala* but not typical Sub (e.g., Sd) genes revealed in this and recent studies. The real Sv only appears at the most caudal levels of the coronal sections (Figures 3K–3M and 3P–3R). Finally, it is also worth mentioning that the borders between the Sub and the PS and between the PS and CA1 are oblique with variable orientation at different levels (Figures 3A–3M), making it very difficult to restrict the neuronal tracer or drug injections in only one region. All these findings are confirmed in sequential sagittal ISH sections of *Calbl* (marker for the PS; Figures S4A–S4H) and *Bcl6* (marker for the Sub; Figures S4I–S4O). It is interesting to find that the PSv and Sv occupy the superficial and deep pyramidal layers, respectively, at level H *(Calbl)* or level P (*Fn1*, another marker for the Sub; Figure S4P) of the sagittal sections.

Distinct Brain-wide Projection Patterns of the Sub and PS

To determine whether the Sub and PS have similar, distinct, or mixed projection patterns, we compared brain-wide projection targets of the Sub and PS by separating Sub- and PS-injected cases. While most previous connectional studies used wild-type (WT) animals and traditional neuronal tracers, we have mostly made use of Cre-driver mice (Table S2) in this study to avoid potential fibers of passage contamination and to make the evaluation of injections and interpretation of results easier. As expected, it is extremely difficult to restrict rAAV (recombinant adeno-associated virus) injections in the Sub or PS of WT mice without leakage into the adjoining PS or Sub. Among many injections involving the Sub of WT mice, we identified only four cases with injection sites mainly in the Sub (but not the PS). In Cre-driver mice, selectively targeting the Sub is much easier. For example, in 77vb2-F2A-CreERT2 and *Grik4-Cre* mice, where the gene driving Cre is expressed only in the Sub but not the PS (Figure 2B), the effective injection site would only be in the Sub even if the injection covers both the Sub and adjoining PS because Cre-dependent GFP expression is only present in Cre-expressing neurons. We identified 16 Cre mice with effective injection sites in the Sub but not the PS. The overall distribution of labeled axon terminals in the target regions of the Sub is shown in Table S2. Briefly, Sd injections resulted in strong terminal labeling in the RSg, PaS, PrS, Pro, MEC, MM (medial mammillary nucleus), AV (anteroventral thalamic nucleus), AM (anteromedial thalamic nucleus), and Re with weaker labeling in the LS (lateral septal nucleus) (Figures 4A and S5A(1)–S5I(1); for terminology and abbreviations, see STAR Methods). In Sv-in-jected cases, labeled terminals were found in the same target regions as in the Sd cases but at differential DV locations, except in the Re (Figures 4B–4D, 5A–5O, and S5A(2)–S5I(2)). In the Re, projections from both the Sd and Sv converge in the dorsolateral part (Figures S5J(1) and S5J(2)). In all Sub-injected cases, little or no labeling was detected in the PL-IL, PRC (perirhinal cortex), VS (ACB + OT), BST, AON (anterior olfactory nucleus), AOB (accessary olfactory bulb), amygdaloid nuclei, and most of the hypothalamic regions except for the MM (Figures 4, 5, and S5). Taken together, the main targets of the Sub include the RSg, PaS, PrS, Pro, MEC, AV, AM, MM, and Re (target set A).

A total of 12 PS-injected cases were selected and analyzed. The injection sites in these cases were localized in the PSd and PSv (but not in the Sub) with or without involvement in other adjoining regions (Table S2). In three PSd cases, labeled axon terminals were seen in the IL, LEC, VS, LS, AON, and amygdala (Figure 4E), with few in the PRC, Re, and hypothalamus. In nine PSv cases, strongly labeled terminals were observed in the IL-PL, LEC, VS, LS, AON, amygdala, PRC, BST, PaT, PT, Re, and hypothalamic nuclei (Figures 4F–4H, 4L, 4M, and 6), with much less labeling in the MEC and MM. In the Re, labeled terminals were concentrated in the ventromedial portion (Figure 6K). In Drd3-Cre_KI196, Vipr2-Cre_KE2, and WT cases, labeled terminals were also observed in the AM but not in the AV (Figures 4F and 4H). In Syt17-Cre_NO14, strong terminal labeling was seen in the AOB (Figure 6F), although in other cases, this labeling was very weak and sparse. In all 12 PS cases, little or no terminal labeling was detected in the main target regions of the Sub (i.e., RSg, PrS, Pro and AV). Overall, the main targets of the PS include the IL, LEC, VS, LS, AON, PRC, BST, PaT, PT, Re, amygdala, and hypothalamic nuclei (target set B; Tables S2 and S3).

Cell-Type-Specific Projections of the Sub and PS

As demonstrated above, both the Sub and the PS have at least two major excitatory neuronal subclasses located in the pyramidal and polymorphic cell layers, respectively. Here, we explore if these two subclasses have different projection patterns. We first divided the Cre mice with Sub injections into two groups: one with injections in both the Spy and Spo and another only in the Spy (Table S2). In the former (e.g., Trib2-2A-CreERT2, *Grm2*-Cre_MR90, and *Slc17a6-IRES-Cre* lines; Figures 4C and S6T–S6W), labeled axon terminals were seen in the RSg, PrS, PaS, MEC, MM, and Pro (target set A1) as well as in the AV, AM and Re (target set A2). In the latter group, however, labeled terminals were only seen in target set A1 (e.g., *Grik4-Cre* line; Figure 4B), indicating that target set A2 is mainly innervated by the Spo rather than the Spy. Consistently, in cases with injections mostly restricted in the Spo, labeled terminals were mostly observed in target set A2 (e.g., *Plxndl*-Cre_OG1 and Drd1a-Cre_EY262 lines; Figures S6R and S6S). Interestingly, the most distal portion of the Spo (close to the PrS) appears to project to the AV but not AM, indicating that the AM is mainly innervated by the more proximal part of the Spo. In fact, when an injection was restricted in the most distal portion of the Spo in the Sd of a *Slc17a7-IRES*-Cre mouse, labeled terminals were only seen in the AV and not in the AM (Figure S6Y). By comparing terminal labeling in the Re of Trib2-2A-CreERT2 and *Slc17a7-IRES*- Cre mice, it is obvious that the Re receives inputs from *Slc17a7-Cre* but not *Trib2-Cre* neurons. The Re inputs appear to derive mainly from the Spo, with fewer from the Spy since strong terminal labeling was observed in the Re of *Grm2*-Cre_MR90 mouse, in which *Grm2* is predominantly expressed in the Spo (Figures S6E and S6T). Consistently, much weaker terminal labeling was observed in the Re of *Grik4-Cre* and Scnn1a-Tg3-Cre mice, in which *Scnn1a* is predominantly expressed in the Spy with less in the Spo (Figures S6F and S6U).

We also found that the PSpy and PSpo have different projection patterns. Only injections contained in the PSpo resulted in terminal labeling in the thalamic nuclei AM and Re, although the PSpy projects to a wide range of brain regions (see above section). For example, no labeled terminals were found in the AM and Re in Syt17-Cre_NO14, *Ntng2*-

IRES2-Cre, *Calb1-T2A*- dgCre, and Ppp1r17-Cre_NL146 mice (Figures 4E, 4G, and 4L), in which the gene driving Cre is not expressed in the PSpo (Figures 1D and 2S). On the other hand, clear projections to the AM and Re were observed in Drd3-Cre_KI186 and *Vipr2*-Cre_KE2 mice (Figures 4F and 4H), in which the gene driving Cre is expressed in the PSpo (Figures S6G and S6H). Another interesting finding is that the PS (both the PSpy and PSpo) did not project to the AV, which instead received strong inputs from the Spo. It is also worth noting that axon projections to the PaT-PT were detected in *Syt17*-Cre_NO14, *Ntng2*-IRES2-Cre, and *Calbl*-T2A-dgCre (PSpo negative; Figures 4G and 4L), but not in *Slc17a6-IRES-Cre* (PSpo positive; Figure S6X), mice, indicating that these projections likely originate from the PSpy with few or none from the PSpo.

We used Slc17a6-IRES-Cre (expression in the PSpy-de), *Calb1*-T2A-dgCre (expression mainly in the PSpy-su), and *Ntng2-IRES2-Cre* lines to compare the projection patterns of these cell types in the PSpy. In Slc17a6-IRES-Cre mice with injections in both the Sub and the PS, heavy projections to the LS, VS, and anterior hypothalamic region were detected (Figure S6X), in addition to projections to major Sub targets (i.e., target set A). These results indicate that the PSpy-de gives rise to strong projections to the LS, VS, and anterior hypothalamus since injections restricted in the Spy of *Slc17a6*- IRES-Cre mice resulted in little or no terminal labeling in those three targets (Figures S6V and S6W). In all *Slc17a6-IRES-Cre* mice with injections contained in the PSpy-de, little or no terminal labeling was observed in the amygdala. In contrast, in *Calbl*- T2A-dgCre mice, obvious projections to the LS, VS, and amygdaloid nuclei [mainly BL (basolateral nucleus)] were observed with little or no labeling in the hypothalamus (Table S2), suggesting some PSpy projections to the amygdala originate from *Calb1-ex*- pressing neurons in the PSpy-su. In Mng2-IRES2-Cre (expressed in both the PSpy-su and PSpy-de), dense axon terminals were found in all PS target regions (i.e., target set B) including the BL, BM, and many other amygdaloid nuclei (Table S2). This suggests that *Ntng2*-expressing neurons in the PSpy-de project to the BM while those in the PSpy-su project to the BL.

Topographic Projections of the Sub along the DV Axis

rAAV injections restricted in either the Sd or Sv resulted in axon terminal labeling in essentially the same set of target regions (i.e., target set A). However, the terminals were differentially distributed in their target regions. For example, labeled terminals from the Sd were detected in the most rostrodorsal part of the RSg; the most dorsal part of the LS, PrS, and PaS; the most dorsorostral part of the MM; the most dorsolateral part of the MEC (Figures S5A(1)–S5I(1)); and the most caudolateral AM-AV (Figures S7C(0)–S7C(4)). Labeled terminals from the Sv were observed in the most caudoventral part of the Rsg; the most ventral part of the LS, PrS, and PaS; the most ventrocaudal part of the MM; the most ventromedial part of the MEC (Figures S5A(2)–S5I(2)); and the most rostromedial AM-AV (Figures S7E(0)–S7E(4)). When the injections were placed in the intermediate portion of the Sub, labeled terminals were distributed in the regions between those derived from the most dorsal and most ventral parts of the Sub (Figures S7D(0)–S7D(4)). In brief, the Sub displays topographic rather than differential projections to their major targets along the DV axis (i.e., target set A; Table S3), with the exception of the Re, where the terminals from both the Sd

and Sv appear to converge (Figures S5J(1) and S5J(2)). In Bienkowski et al. (2018), the dorsal and ventral Sub were reported to project to target sets A and B, respectively.

Differential and Topographic Projections of the PS along the DV Axis

Since differential projections of the Sub along the DV axis were not observed, we hypothesize that the DV difference of the projections from the loosely defined Sub reported in literature probably originates from the PS. Thus, we compared the terminal distribution in the main target regions of the PSd and PSv (Figures 4 and S7). The PSv heavily projects to the LEC, LS, VS, amygdala, and many hypothalamic nuclei and moderately to the PRC, IL, AM, PT, PaT, AON, MM, and BST. In contrast, terminal labeling originated from the PSd was much less dense in the above mentioned PS target regions such as the LS, VS, LEC, and amygdala and almost absent in other target regions such as the IL, BST, AON, MM, and hypothalamus (Table S2).

In addition to differential DV projections, topographic projections were also observed from the PS to some target regions such as the AM, IL, LS, VS, and BLof the amygdala. Specifically, the PSd projects to the caudolateral AM (Figures S7A(0)–S7A(4)), ventral IL, dorsomedial LS, lateroventral VS (Figures S8A–S8D), and lateral BL (Figures S8I–S8K). In contrast, the PSv projects to the rostromedial AM (Figures S7B(0)–S7B(4)), dorsal IL, ventrolateral LS, mediodorsal VS (Figures S8E–S8H), and medial BL (Figures S8L–S8N).

Efferent Projections of Adjoining CA1 and MEC

Given that the PS is next to CA1, we next examined the efferent projections of CA1 compared to those of the PS and Sub. CA1d projects strongly to the Sd, MEC (the most dorsal EC), and dorsal LS and lightly to the PSd, but not to the VS and the amygdala (Figures 4I, S9Q, and S9R). This is consistent with previous findings in mouse (e.g., Roy et al., 2017), but CA1d was sometimes reported to project to the LEC (e.g., Cenquizca and Swanson, 2007; in rat). The difference is likely due to inconsistent criteria for the definition of the LEC, MEC, and their borders across different labs, and this needs to be further studied. In contrast to CA1d, CA1v projects strongly to the Sv, PSv, MEC, and ventral LS with weak projections to the IL, PRC, caudal hypothalamus, LEC, IL, AON, VS, and amygdala (Figures 4J, 4K, and S9S–S9U; all are also the targets of the PSv). In cases with injections also including the adjoining PSv (e.g., Figure 4L), heavy terminal labeling was observed in the IL, AON, VS, LS, LEC, and amygdala with moderate labeling in the BST, PRC, PT and caudal hypothalamus. In all cases, no labeling was found in target regions of the Sub such as the RSg, Pro, PrS, PaS, MM, and AV. Therefore, CA1v displays a similar projection pattern but with much less density and intensity when compared to the PSv (Figures 4I–4L; Table S2). In addition, CA1v projections to the amygdala mainly target the BL with few to other amygdaloid nuclei.

As shown in Figure S4, the Sv adjoins the MEC caudally via a thin layer of white matter. To determine if the MEC projects to some Sub or PS target regions, we examined six cases with injections restricted in the MEC. In two Cux2-IRES-Cre and two *Slc17a6-IRES-Cre* cases in which the gene driving Cre expression is restricted to L2 and L3 of the MEC, the injections contained only the MEC (but not the Sv) and resulted in heavily labeled terminals in the

molecular layer of the LEC, DG, CA1, Sv, and PaS, with light labeling in the AON, IL, and OT. In three WT cases (Table S2), however, the injections also contained L5 and L6 of the MEC and resulted in heavy terminal labeling in the postrhinal cortex, caudate-putamen, amygdala (mainly BL and AHi), amygdalostriatal transition area, AV, LD, NLOT, VS, and claustrum, with lighter labeling in the hypothalamus. Therefore, previously reported Sv projections to the amygdala, LD, VS, and hypothalamus may instead be derived from deep MEC that may be contained in Sub injections.

Brain-wide Differential Afferent Projections to the Sub and PS

Since the Sub and PS have differential efferent projection targets, we next examined whether the Sub and PS receive differential afferent inputs. The amygdala projects to the PSv with no labeling in the Sv (Figures S9A–S9D). The CA3d and CA3v project to the PSd and PSv, respectively, with no projections to the Sub (Figures S5K–S5M, S9I, and S9J). LEC projections mainly target the PS rather than the Sub (in the Sub, mainly fibers rather than axon terminals were observed; Figures S9E–S9H). Injections in the Re result in strong terminal labeling in the PSv with much less labeling in the Sub (Figures S9K and S9L). In contrast to LEC injections (Figures S9G and S9H), ventral MEC injections resulted in heavy terminal labeling in the Sv with much less labeling in the PSv (Figures S9M and S9N); in the PSv, mostly fibers rather than terminals were observed. Interestingly, the dorsal MEC tends to project to the Sd with no labeling in the Sv (Figure S9P). Finally, the AV of the thalamus projects to the Sub rather than the PS, and the labeled terminals are distributed in both the dorsal Spo (Figure S9O) and the ventral Spo (not shown). Quantitative analysis reveals that the Sub receives its inputs mainly from the MEC, PrS, and AV, in addition to heavy CA1 inputs, while the PS mainly receives its inputs from the amygdala, LEC, CA3, Pir, and Re, in addition to heavy CA1 inputs (Figure S9V).

DISCUSSION

The present study has identified 27 transcriptomic clusters/cell types in the Sub regions, which include the Sub, PS, and HA. Using gene markers for specific cell types in these three regions, we have accurately delineated the borders between them along the full DV axis and found that the dorsal and ventral Sub regions are occupied mainly by the Sub and PS, respectively (Figures 7 and S10). These findings are critical to the accurate and consistent localization of neurons and injections as well as to data interpretation. With these findings, we have demonstrated that both the Sd and Sv project to the same target regions with topographic organization. This challenges the traditional concept that the Sd and Sv have differential projections. Furthermore, we have found the most ventral Sub region actually belongs to the PSv and displays strong connections with structures critical to motivation, emotion, reward, stress, anxiety, and fear. The distinction and DV difference in sizes of the Sub and PS along the DV axis also enable consistent interpretation of anatomic, molecular, functional, and behavioral results in the literature and in different species.

Other findings of the present study include the following (Figures 7A and 7B; Table S2): (1) the PS projects to the claustrum/ endopiriform nucleus and accessory olfactory bulb; (2) the Sub, but not the PS, projects to the area prostriata (Pro; see Lu et al., 2020), which is heavily

involved in spatial processing; (3) the Sub projects to both the AV and AM, while the PS projects only to the AM; (4) the Sub projects to the dorsolateral Re, while the PS projects to the ventromedial Re; (5) the CA3 projects to the PS but not to the Sub; (6) the dorsal CA1 projects to L6 of the PrSd (PoS); and (7) many projection patterns of different cell types of the Sub, PS, and CA1 have been revealed using many different Cre lines.

Transcriptomic Cell Types of Excitatory Neurons in the Sub and PS

Cembrowski et al. (2018b) recently explored the transcriptomic cell types of excitatory neurons in the Sub regions using scRNA-seq. With a smaller sample size (n = 1,150 cells), they observed eight clusters (with an additional one in CA1: C7). In comparison, our study revealed 27 clusters with a sample size of 8,648 cells from the same Sub regions. Based on our confusion matrix analysis and the marker genes, their nine clusters can be mapped and partially overlap with the overall 29 clusters revealed in this study (Figure S2A). We find 9,14, and 4 clusters or cell types within the Sub proper, PS, and HA, respectively. PSpy neurons exhibit greater heterogeneity (Figure 1C). Cells in the PSpy-su1 (the most superficial portion) are transcriptionally closer to neurons in the HApy. The PSpy-su2 is closer to the PSpy-de, and both are closer to CA1py. Overall, at the transcriptional level, the PSpy is closer to CA1py than to the Spy, supporting our conclusion that the Sub and PS are two distinct entities with differential molecular architecture, neural circuits, and functional correlation (see below).

Molecular Dissection of the Sub and PS and Their Borders

Although the monkey PS could be clearly identified with the help of AChE stain by many researchers (Barbas and Blatt, 1995; Ding, 2013; Fudge et al., 2012; Saunders et al., 1988; Yukie, 2000), reliable and precise identification of the rodent PS has been difficult due to the curvature of the HF and the lack of reliable markers. Consequently, the PS region has been treated as part of the Sub in most rodent literature. However, the existence of a distinct rodent PS has been re-emphasized recently, based on a combined analysis of comparative, connectional, neurochemical, and molecular data (Ding, 2013). In this study, we have assigned transcriptional cell types to anatomical locations and found that the general Sub contains at least three distinct regions: the PS, Sub proper, and HA. Furthermore, the borders, extent, and topography of the Sub, PS, and HA along the DV axis are consistently and reliably defined based on distinct molecular markers revealed from the transcriptome. We further find that the sizes (widths) of the Sub and PS decrease and increase, respectively, along DV levels and that the Sub and PS display generally distinct afferent and efferent projections (Figure 7).

Based on these findings, many confusing and conflicting results in previous rodent studies can be explained with the introduction of the PS concept and the precise and reliable demarcation of its border. For example, we found that the region previously labeled as the ventral Sub in most rodent literature in fact is the ventral PS because it expresses transcriptionally identified marker genes for the PS rather than those for the Sub. Consistent with this conclusion, this region, although called the “ventral Sub,” was found to project to the IL, VS, AON, BST, PRC, and many amygdaloid and hypothalamic nuclei (Bienkowski et al., 2018; Cullinan et al., 1993; Kishi et al., 2006; McDonald, 1998; Swanson and Cowan,

1977), all of which are typical target regions of the PS revealed in the present study. We conclude here that it is the PS rather than the Sub predominantly projecting to the structures critical for motivation, emotion, reward, stress, anxiety, and fear (Aggleton 2012; Andrzejewski et al., 2006; Herman and Mueller, 2006; O'Mara et al., 2009; Potvin et al., 2006; Subhadeep et al., 2017).

Many previous studies in rodent divided the Sub (mainly the dorsal Sub) into the distal and proximal Sub instead of the Sub and the PS (Figure S10; Aggleton, 2012; Aggleton and Christiansen, 2015; Witter, 2006). The distal and proximal Sub were originally used to describe the locations of injection sites and labeled neurons in the dorsal Sub (e.g., Naber and Witter, 1998; Witter, 2006; Witter et al., 1990), with the proximal Sub closer to CA1 and the distal Sub farther from CA1 but no specific markers for each. Recently selected gene markers were introduced to mark the distal and proximal Sub (S-dis and S-pro) (Cembrowski et al., 2018a, 2018b) or the Sub and the PS (Bienkowski et al., 2018; Ding, 2013), mostly for the dorsal Sub. Connectivity data appear to support this subdivision of the dorsal Sub (Bienkowski et al., 2018; Cembrowski et al., 2018a; Witter, 2006). However, in the ventral Sub region, the distal and proximal Sub do not appear to be dividable (Cembrowski et al., 2018b) or could not be divided into the S-dis and S-pro (Bienkowski et al., 2018). In fact, the distal and proximal Sub express Sub and PS genes such as *Nts* and *Ntng2*, respectively, in the dorsal part. In the ventral part, however, both the distal (away from CA1) and proximal (close to CA1) regions express PS genes (e.g., *Ntng2* and *S100a10).* At more caudal levels, it is even harder to demarcate the distal and proximal Sub. Therefore, the concept of the distal and proximal Sub cannot be clearly applied to the ventral Sub region. Here, using distinct markers consistently defined for Sub and PS cell types from ourtranscriptomic taxonomy, we have revealed that the ventral Sub region actually belongs to the PSv (Figures 3, 7C, S4, and S10) rather than to the Sv.

Untangling of the Wiring Circuits of the Sub and PS

Guided by reliable boundaries of the Sub and PS along the DV axis, we are able to untangle the wiring circuits of the Sub and PS. Sub projections are mostly observed in the RSg, PrS, PaS, MEC, Pro, LS, Re (dl), AV, AM, and MM (target set A). PS projections are found in the IL, LEC, VS, LS, Re (vm), AON, BST, PRC, PaT-PT, claustrum, amygdala, and almost all hypothalamic regions (target set B; Figure 7). Thus, the Sub and PS basically project to distinct sets of brain regions with only a few exceptions. Three possible exceptions are in the LS, AM, and MM, where both Sub and PS projections may converge. This is in contrast to previous studies showing mixed (not distinct) projection patterns of the Sub, which may be due to the mixing of two different entities (PS and Sub) into one Sub; the oblique border between the two entities and the small size of each; and/or the leakage of tracers into neighboring regions or underlying white matter. Cre-dependent viral tracing used in this study could increase the accuracy of targeting specific regions and cell types.

The finding of distinct projection patterns of the Sub and PS is consistent with previous retrograde tracing results from the dorsal distal and proximal 'Sub." For example, when retrograde tracers were injected in the IL, VS, BST, amygdala, and PRC, labeled neurons were found only in the proximal Sub region, corresponding to the PS in this study (Christie

et al., 1987; Ishizuka, 2001; Kishi et al., 2006; Ottersen, 1982; Phillipson and Griffiths, 1985; Shi and Cassell, 1999; Veening, 1978; Weller and Smith, 1982; Witter, 2006; Witter et al., 1990). When retrograde tracers were injected into the RSg and AV, labeled neurons were only observed in the distal Sub, corresponding to the Sub proper in this study (Christiansen et al., 2016; Meibach and Siegel, 1977b; Wyss and Van Groen, 1992). Consistently, afferent projections to the Sub and PS were found to originate generally from differential brain regions (Figure S9). The PS receives major inputs from the CA3, CA1, LEC, piriform cortex, midline thalamic nuclei, medial septal nucleus, and amygdala, while the Sub receives inputs mainly from the CA1, MEC, PrS, and AV-AM (Figure 7; Ding, 2013; Roy et al., 2017).

Taken together, the Sub and PS defined in this study apply well to both the dorsal and the ventral Sub regions and display distinct wiring circuits, with the PS having more widespread inputs and outputs than the Sub. The Sub connects with regions heavily involved in spatial processing and navigation. In contrast, the PS connects with limited cortical regions but many subcortical regions that have strong association with motivation, reward, emotion, fear, and stress. It is worth mentioning that one of the many PS targets (i.e., the LEC) appears to be involved in many brain functions including learning, memory, reward, emotion, and multisensory integration (Doan et al., 2019; Hutter et al., 2013; Leal et al., 2017; van Strien et al., 2009).

Topographic and Differential Projections of the Sub and PS along the DV Axis

With the exception of the Pro and Re, all other main target regions of the Sub receive clear topographic projections from the Sub. These findings are consistent with previous retrograde tracing results in rat (Honda and Ishizuka, 2015; Meibach and Siegel, 1977a; Wyss and Van Groen, 1992) and mouse (Cembrowski et al., 2018a) because retrogradely labeled neurons in these studies were actually restricted in the region corresponding to the Sub proper. Moreover, the dorsal and ventral limits of the Sub are highly consistent with the dorsal and ventral borders revealed with the molecular markers in the present study. Thus, the topographic projections from the Sub to its main target regions such as the RSg, MEC, and PrS could also be used to confirm the most dorsal and the most ventral limits of the Sub (Figure S5).

In previous studies, a connectional difference of the Sub and CA1 along the DV axis was frequently reported (Strange et al., 2014). In this study, we found this DV difference exists for PS and CA1 projections, but almost not for Sub projections. The main reason for this discrepancy is that many previous studies did not recognize the PS but treated it as part of the Sub (Canteras and Swanson, 1992; Cullinan et al., 1993; Swanson and Cowan, 1977) and/or did not use reliable markers to distinguish the Sub from the PS. Using reliable molecular markers, we find that the PS and adjoining CA1 have obvious differential DV projections. These difference include the following: (1)the ventral PS has dense, while the dorsal PS has few or no, projections to the AON, BST, and hypothalamus; and (2) the ventral PS has much stronger projections to the VS, LS, and amygdala than the dorsal PS does. Interestingly, PS projections to the VS, IL, LS, and BLof the amygdala show rough topographic organization.

Another important finding of the present study is that the Sub and PS dominate the dorsal and ventral Sub region, respectively. In fact, we found the most dorsal region lacks the PS (Figures 3A, S4A, and S4B), while the most ventral region lacks the Sub (Figures 3H–3J, 3N, 3O, S4F, S4G, S4N, and S4O), and the size and extent of the Sub and PS display opposite DV gradients (Figure 7C). These findings indicate that the dorsal Sub lesion mainly damages the Sub, while the ventral Sub lesion mainly damages the PS. In addition, the dorsal PS/CA1 gives rise to many fewer projections to the IL-PL, VS, and amygdala and almost no projections to the BST and hypothalamus. These results together suggest that the dorsal Sub lesion would mainly display impaired spatial processing and navigation, while the ventral Sub lesion would mainly show impaired reward, emotion, motivation, fear, and stress response. This is consistent with commonly reported functional differences between the dorsal and ventral “Sub” regions (O’Mara et al., 2009; Strange et al., 2014).

Functional Implications

Consistent with many previous works, the present study demonstrates that the main targets of Sub projections include the RS (RSg), MEC, PrS, PaS, MM, ATN (AV and AM), and Re. Lesions in these structures and in the dorsal Sub heavily impair spatial memory, orientation, and navigation (Aggleton and Christiansen, 2015; Cembrowski et al., 2018a). Physiologically, these structures contain cells sensitive to spatial information such as grid cells, head direction cells, and border cells (Hafting et al., 2005; Jankowski et al., 2014; Lever et al., 2009; Olson et al., 2017; Taube, 2007). The topographic organization of Sub projections to the main target structures (rat, Honda and Ishizuka, 2015; Wyss and Van Groen, 1992; mouse, this study) and gradient gene expression along the DV axis (Strange et al.,2014) of the HF including the Sub also appear to support spatial computation.

Many previous studies reported ventral Sub projections to the IL, LEC, PRC, LS, VS, BST, AON, Pat-PT, amygdala, and hypothalamus (Bienkowski et al., 2018; Ding, 2013; Jin and Maren, 2015). Lesions or simulations in these structures and in the ventral Sub resulted in changed feeding and social behaviors and stress responses (Aqrabawi et al., 2016; Cassel et al., 2013; Farrell et al., 2010; Hsu et al., 2014; Mannella et al., 2013; Parfitt et al., 2017; Riaz et al., 2017; Sweeney and Yang, 2015, 2016; Vranjkovic et al., 2017; Wassum and Izquierto, 2015). In this study, we recognize that this ventral Sub actually belongs to the PSv based on gene expression and connectivity patterns. Recently, the “CA1v” region, corresponding to the PSv and adjoining CA1v of the present study, has been found to contain a lot of “anxiety” cells, which mainly project to the hypothalamus and drive anxiety-related avoidance behavior and aversion (Jimenez et al., 2018). This same region also contains another set of cells that project to the amygdala and mainly modulate contextual fear memory encoding and retrieval. One striking finding of the present study is that the PS contains 14 clusters (cell types). We hypothesize that different cell types might innervate a subset of target regions of the PS and thus modulate different functions in fear, anxiety, reward, and motivation. For example, Slc17a6-expressing neurons in the PSpy-de do not appear to innervate the amygdala, while *Calbl*-expressing neurons in the PSpy-su do (Table S2). Therefore, *Calbl*- Cre mice could be used to specify the function of the PS projections to the amygdala in future studies.

In summary, as demonstrated in this study, the Sub and the PS are two distinct regions with differential transcriptome, molecular signature, connectivity, and functional correlation along the entire DV axis. The benefits of introducing/rescuing the term PS for rodent brain include at least the following aspects: (1) enable consistent description of the Sub and PS across species (see Ding [2013] for evidence); (2) match well to distinct molecular markers and connectivity of the Sub and PS along the DV axis; (3) correlate well with differential functions of the Sub and PS; (4) enable accurate targeting and description for future lesion, injection, stimulation, and recording studies; and (5) facilitate accurate evaluation and interpretation of the results from animal models of related diseases.

STAR★METHODS

RESOURCE AVAILABILITY

Lead Contact—Further information and requests for resources and reagents should be directed to and will be fulfilled by the Lead Contact, Song-Lin Ding (songd@alleninstitute.org).

Materials Availability—This study did not generate unique reagents.

Data and Code Availability—Allen Brain Atlas ISH data and Allen Mouse Brain Connectivity Atlas data are available at Allen Institute data portal (https://portal.brain-map.org). Single-cell transcriptomic data are deposited to the Neuroscience Multi-omic (NeMO) Data Archive with an identifier nemo:dat-61rv7xg (https://assets.nemoarchive.org/dat-61rv7xg). R packages for the consensus clustering of single-cell transcriptomic data are available on GitHub at https://github.com/AllenInstitute/scrattch.hicat.

EXPERMENTAL MODEL AND SUBJECT DETAILS

Both male and female mice ≥ P56 were utilized for all experiments. All animals were housed 3-5 per cage and maintained on a 12-hour light/dark cycle, in a humidity- and temperature-controlled room with water and food available *ad libitum.* All experimental procedures were approved by the Allen Institute Animal Care and Use Committee and conform to NIH guidelines.

Wild-type (C57BL/6J; n = 20) and Cre driver transgenic mice (n = 82) at postnatal day (P) 56 ± 3 were used in tracing study. The Cre lines mainly includes Calb1-T2A-dgCre (n = 3), Cux2-IRES-Cre (n = 8), Dlg3-Cre_KG118 (n = 1), Drd1a-Cre_EY262 (n = 1), Drd3-Cre_KI196 (n = 3), Etv1-CreERT2 (n = 3), Gad2-IRES-Cre (n = 3), Gal-Cre_KI87 (n = 1), Gpr26-Cre_KO250 (n = 4), Grik4-Cre (n = 8), Grm2-Cre_MR90 (n = 1), Grp-Cre-KH288 (n = 3), Htr1a-IRES2-Cre (n = 1), Kcnc2-Cre (n = 1), Ntng2-IRES2-Cre (n = 3), Otof-Cre (n = 3), Pcdh9-Cre_NP276 (n = 2), Plxnd1-Cre_OG1 (n = 2), Ppp1r17-Cre_NL146 (n = 5), Rbp4-Cre_KL100 (n = 1), Rorb-IRES2-Cre (n = 2), Scnn1a-Tg3-Cre (n = 3), Sim1-Cre_KJ18 (n = 1), Slc17a6-IRES-Cre (n = 5), Slc17a7-IRES2-Cre (n = 4), Syt17-Cre_NO14 (n = 6), Trib2-2A-CreERT2 (n = 1) and Vipr2-Cre_KE2 (n = 3). These lines were generated at the Allen Institute or imported from external sources (see Harris et al., 2014; Daigle et al.,

2018; Key Resources Table) and examples of Cre expression in Sub, PS and adjoining regions from these lines were shown in Figure S6; Table S2.

METHODS DETAILS

Terminology and Abbreviations—The mouse brain atlas of Paxinos and Franklin (2012) and Allen Mouse Brain CCFv3 (Wang et al., 2020) were used in this study. Many structure terminologies are the same or similar in both atlases. See the list below for details.

	This paper	Allen CCFv3
Ventromedial prefrontal Cortex	PFvm	
Infralimbic cortex	IL	ILA
Prelimbic cortex	PL	PL
Retrosplenial cortex	RS	RSP
Granular retrosplenial cortex	RSg	RSPv
Granular retrosplenial cortex, dorsal part	RSgd	not defined
Granular retrosplenial cortex, ventral part	RSgv	not defined
Other cortex		
Accessory olfactory bulb	AOB	AOB
Accessory olfactory bulb, granule layer	AOBgr	AOBgr
Anterior olfactory nucleus	AON	AON
Piriform cortex	Pir	PIR
postrhinal cortex	POR	VISpor
Perirhinal cortex	PRC	PERI
Area prostriata	Pro	APr
Entorhinal cortex	EC	ENT
Lateral entorhinal cortex	LEC	ENTl
Medial entorhinal cortex	MEC	ENTm
Subicular complex		
Pyramidal layer	py	not defined
polymorphic layer	po	not defined
Stratum lacunosum-moleculare	m-l	not defined
Subiculum	S (Sub)	SUB
Dorsal subiculum	Sd	not defined
Ventral subiculum	Sv	not defined
Pyramidal layer of subiculum	Spy	not defined
polymorphic layer of subiculum	Spo	not defined
Prosubiculum	PS (ProS)	ProS
Dorsal prosubiculum	PSd	not defined
Dorsal prosubiculum	PSv	not defined
pyramidal layer of Prosubiculum	PSpy	not defined

	This paper	Allen CCFv3
pyramidal layer of Prosubiculum, deep part	PSpy-de	not defined
pyramidal layer of Prosubiculum, superficial part	PSpy-su	not defined
polymorphic layer of Prosubiculum	PSpo	not defined
Presubiculum	PrS	PRE
Dorsal presubiculum (~postsubiculum)	PrSd	POST
Ventral presubiculum	PrSv	PRE
Parasubiculum	PaS	PAR
Parasubiculum, dorsal part	PaSd	not defined
Parasubiculum, ventral part	PaSv	not defined
Hippocampo-amygdalar transition area	HA	HATA
Hippocampal formation	HF	
Dentate gyrus	DG	DG
Field CA1 of hippocampus	CA1	CA1
Field CA1 of hippocampus, dorsal part	CA1d	not defined
Field CA1 of hippocampus, ventral part	CA1v	not defined
stratum radiatum of field CA1	ra	not defined
Field CA3 of hippocampus	CA3	CA3
Field CA3 of hippocampus, dorsal part	CA3d	not defined
Field CA3 of hippocampus, ventral part	CA3v	not defined
Striatum		
Accumbens nucleus	ACB	ACB
Caudoputamen	CP	CP
Islands of Calleja, major island	ICjM	not defined
Olfactory tubercle	OT	OT
Ventral striatum	VS	not defined
Amygdalar complex	Amy	
Lateral amygdaloid nucleus	La	LA
Basolateral amygdaloid nucleus	BL	BLA
Basolateral amygdaloid nucleus, anterior part	BLA	BLAa
Basolateral amygdaloid nucleus, posterior part	BLP	BLAp
Basomedial amygdaloid nucleus	BM	BMA
Basomedial amygdaloid nucleus, anterior part	BMA	BMAa
Basomedial amygdaloid nucleus, posterior part	BMP	BMAp
Central amygdaloid nucleus	Ce	CEA
Central amygdaloid nucleus, lateral division	CeL	CEAl
Central amygdaloid nucleus, medial division	CeM	CEAm
Medial amygdaloid nucleus	Me	MEA
Medial amygdaloid nucleus, dorsal part	MeD	not defined
Medial amygdaloid nucleus, ventral part	MeV	not defined

	This paper	Allen CCFv3
Posterior cortical amygdaloid nucleus	CoP	COAp
Bed nuclei of the stria terminalis	BST	BST
Amygdalohippocampal area	AHi	PA (Post. Amyg. n.)
Amygdalopiriform area	APir	TR (Transition area)
Amygdalostriatal transition area	ASTA	not defined
Thalamus		
Anterodorsal thalamic nucleus	AD	AD
Anteromedial thalamic nucleus	AM	AM
Anteroventral thalamic nucleus	AV	AV
Laterodorsal thalamic nucleus	LD	LD
Mediodorsal thalamic nucleus	MD	MD
Paraventricular thalamic nucleus	PaT	PVT
Paratenial thalamic nucleus	PT	PT
Reuniens thalamic nucleus	Re	RE
Zona incerta	ZI	ZI
Medial geniculate nucleus	MG	MG
Xiphoid thalamic nucleus	Xi	Xi
Hypothalamus (Hypothal, Hypo)	Hy	HY
Anterior hypothalamic nucleus	AHN	AHN
Arcuate hypothalamic nucleus	Arc	ARH
Dorsomedial hypothalamic nucleus	DMH	DMH
Lateral hypothalamic area	LH	LH
Lateral mammillary nucleus	LM	LM
Lateral preoptic area	LPO	LPO
Medial mammillary nucleus	MM	MM
Medial preoptic area	MPA	MPO
Medial preoptic nucleus	MPN	MPN
Paraventricular hypothalamic nucleus	PaH	PVH
Posterior hypothalamic nucleus	PH	PH
Ventral premammillary nucleus	PMv	PMv
Suprachiasmatic nucleus	SCh	SCH
Tuberomamillary nucleus	TM	TM
Tuberomammillary nucleus, dorsal part	TMd	TMd
Tuberomammillary nucleus, ventral part	TMv	TMv
Tuberal nucleus	Tu	TU
ventromedial hypothalamic nucleus	VMH	VMH
Others		
anterior commissure	ac	ac
alveus of hippocampus	alv	alv

	This paper	Allen CCFv3
fimbria of hippocampus	fi	fi
fornix	fx	fx
rhinal sulcus	rs	rs
Claustrum	Clau	CLA
Endopiriform nucleus	En	EP
Lateral seDtal nucleus	LS	LS

Single-cell isolation for SMART-Seq—We adapted a previously described protocol to isolate neurons from the mouse brain (Tasic et al., 2018). Briefly, adult male and female mice (P56 ± 3; n = 4) from the pan-glutamatergic mouse line *Slc17a7-IRES2-Cre;Ai14* were anesthetized with isoflurane and perfused with cold carbogen-bubbled artificial cerebrospinal fluid (ACSF). The brain was dissected, submerged in ACSF, embedded in 2% agarose, and sliced into 250-μm coronal sections on a compresstome (Precisionary). Under microscope, and with reference to Allen Mouse Brain CCF (v3), full DV extent of the regions PS-Sub-HAand PrS-PoS-PaS were microdissected from the 250-μm thick slices with a knife and dissociated into single cells with 1 mg/ml pronase (Sigma, Cat#P6911-1G). Single cells were isolated by FACS into individual wells of 8-well PCR strips containing lysis buffer from the SMART-Seq v4 kit with RNase inhibitor (0.17 U μl-1), immediately frozen on dry ice, and stored at −80°C.

Single-cell isolation for 10X Chromium v2—Adult male and female mice (P56 ± 3; n = 2) from the pan-neuronal mouse line *Snap25-IRES2-Cre;Ai14* were anesthetized, brains were dissected, and 250-μm thick coronal slices were prepared as described for SMART-Seq processing. The entire region containing full DV extent of PS-Sub-HA-PrS-PoS-PaS were micro-dissected out with a knife and a microscope, under which the anatomic borders can be identified, and digested with 30 U/ml papain (Worthington #PAP2) in ACSF for 30 mins at 35°C in a dry oven, with a targeted solution temperature of 30°C. Enzyme digestion was quenched by exchanging the papain solution three times with quenching buffer (ACSF with 1% FBS and 0.2% BSA). Samples were incubated on ice for 5 minutes before trituration. In 1 mL of quenching buffer, the tissue pieces were triturated through a fire-polished pipette, with 600-um diameter opening, approximately 20 times. Tissue pieces were allowed to settle, and the supernatant, which now contains suspended single cells, were transferred to another tube. Fresh quenching buffer (1 ml) was added to the settled tissue pieces, and trituration and supernatant transfer was repeated using 300-um and 150-um fire polished pipettes. Final volume of the single cell suspension is 3 ml. It is possible for small tissue pieces to remain in the original tube after these three rounds of trituration, and these are discarded. To remove excessive debris, the single cell suspension was passed through a 70-um filter into a 15 mL conical tube with 500 μl of high BSA buffer (ACSF with 1% FBS and 1% BSA) at the bottom to help cushion the cells during centrifugation at 100xg in a swinging bucket centrifuge for 10 minutes. The supernatant was discarded, and the cell pellet was resuspended in 1 mL quenching buffer. Cells were passed through 70-um filter again and DAPI (2 ng/ml) was added to the suspension. Cells were isolated using FACS (BD

Aria II) gated on DAPI and tdTomato. In order to increase yield while reducing the sheath volume in the sorted suspension, we sorted on Fine Tune mode which has Yield, Purity, and Phase Mask all set to 0. We divided up the sample so that we could sort 30,000 cells at a time, within 10 minutes, into 5mL tube containing 500 ml of quenching buffer. Each aliquot of sorted 30,000 cells were immediately centrifuged at 230xg for 10 minutes in a swinging bucket centrifuge with 200 ml of high BSA buffer at the bottom for cushion. No pellet can be seen with this small number of cells, so we take out the supernatant and leave behind 35 ml of buffer, in which we resuspended the cells. The resuspended cells are stored at 4°C until all samples have been collected for chip loading on the 10X Genomics controller. Our typical sort takes 30 minutes for three aliquots. We observe more cell death for longer sorts. Typically, one aliquot of 30,000 sorted cells result in a final suspension of 5,000 - 20,000 viable cells for loading onto one port of the 10X Genomics chip.

cDNA amplification and library construction—We used the SMART-Seq v4 Ultra Low Input RNA Kit for Sequencing (Takara, 634894) to reverse transcribe poly(A) RNA and amplify full-length cDNA. We performed reverse transcription and cDNA amplification for 18 PCR cycles in 8-well strips, in sets of 12–24 strips at a time. All samples proceeded through NexteraXT DNA Library Preparation (Illumina FC-131-1096) using NexteraXT Index KitV2 (FC-131-2001). NexteraXT DNA Library prep was performed according to manufacturer's instructions except that the volumes of all reagents including cDNA input were decreased to 0.4 × or 0.5 × by volume. Subsampling of the reads to a median of 0.5 million per cell results in similar gene detection per cell (> 89% of genes detected, data not shown), showing that we detect most of the genes at 2.5 million reads per cell. Details are available in 'Documentation' on the Allen Institute data portal at: http://celltypes.brain-map.org. For 10X Genomics processing, we used Chromium Single Cell 3' Reagent Kit v2 (10X Genomics #120237). We followed manufacturer's instructions for cell capture, barcoding, reverse transcription, cDNA amplification, and library construction. Average sequencing depth was ~59k reads per cell across 9 libraries.

Sequencing data processing and quality control—For the SMART-Seq V4 dataset, fifty-base-pair paired-end reads were aligned to GRCm38 (mm10) using a RefSeq annotation gff file retrieved from NCBI on 18 January 2016 (https://www.ncbi.nlm.nih.gov/genome/annotation_euk/all/). Sequence alignment was performed using STAR v2.5.3 with twopassMode. PCR duplicates were masked and removed using STAR option 'bamRemoveDuplicates'. Only uniquely aligned reads were used for gene quantification. Gene read counts were quantified using the summarizeOverlaps function from R GenomicAlignments package using both intronic and exonic reads, and QC was performed as described inTasicet al. (2018). The 10X dataset was processed using cellrangerv3.0.0 pipeline. Doublet detection was performed using scrattch.hicat doubletFinder function, adapted from the original doubletFinder package v1.0 (McGinnis et al., 2019; https://github.com/chris-mcginnis-ucsf/DoubletFinder) for better efficiency and performance. 10X doublet cells were defined as cells with doublet score greater than 0.3 and removed before clustering. We determined 10X cell class based canonical markers into neurons and non-neuronal cells. For neuronal cells, we selected cells with at last 2000 detected genes, and for non-neuronal cells, we selected cells with at least 1000 detected genes.

Clustering—Clustering for both SMART-Seq and 10X datasets were performed using house developed R package scrattch.hicat (available via github https://github.com/AllenInstitute/scrattch.hicat). In addition to classical single-cell clustering processing steps provided by other tools such as Seurat, this package features automatically iterative clustering by making finer and finer splits while ensuring all pairs of clusters, even at the finest level, are separable by fairly stringent differential gene expression criteria. The package also performs consensus clustering by repeating iterative clustering step on 80% subsampled set of cells 100 times and derive the final clustering result based on cell-to-cell co-clustering probability matrix. This feature enables us to both fine tune clustering boundaries and to assess clustering uncertainty. For differential gene expression criteria between clusters, q1.th = 0.4, q.diff.th = 0.7, de.score.th = 150, min.cells = 20 is used for 10X cells, and q1.th = 0.5, q.diff.th = 0.7, de.score.th = 150, min.cells = 4 is used for SMART-Seq cells. Clusters for each dataset were inspected manually, and based on marker genes, clusters that believed to be outside of subicular complex were eliminated from downstream analysis.

Consensus clustering between 10X and SMART-Seq—To provide one consensus subicular cell type taxonomy based on both 10X and SMART-Seq datasets, we developed an integrative clustering analysis across multiple data modalities, now available via unify function of scrattch.hicat package. Unlike Seurat CCA approach (Butler et al., 2018) and scVI (Lopez et al., 2018), which aim to find aligned common reduced dimensions across multiple datasets, this method directly builds a common adjacency graph using all cells from all datasets, then applies standard Louvain community detection approach for clustering. To build the common graph, we first chose a subset of reference datasets from all available datasets, which either provides stronger gene detection and/or more comprehensive cell type coverage. The key steps of the pipeline are outlined below:

1. **Select anchor cells for each reference dataset.** For each reference dataset, we random sampled up to 5000 cells as anchors. If independent clustering results for the reference datasets are available, we sample at least100 anchor cells per cluster to achieve more uniform coverage of cell type.

2. **Select high variance genes.** High variance genes and PCA dimensions reduction were performed using scrattch.hicat package. PCA dimensions that highly correlated with technical bias such as gene detection or mitochondria gene expression were removed. For each remaining PCA dimension, Z scores were calculated for gene loadings, and top 100 genes with absolute Z score greater than 2 were selected. The high variance genes from all reference datasets were pooled.

3. **Compute K nearest neighbors.** For each cell in each dataset, we computed its K nearest neighbors among anchor cells in each reference datasets based on the high variance genes selected above. Different distance metrics can be selected for computing nearest neighbors between different pairs of datasets. By default, Euclidean distance is used when query and reference dataset is the same. Between different datasets, correlation is used as similarity metrics to select K nearest neighbors.

4. **Compute the Jaccard similarity.** For every pair of cells from all datasets, we compute their Jaccard similarity, defined as the ratio of the number of shared K nearest neighbors (among all anchors cells) over the number of combined K nearest neighbors.

5. Perform Louvain clustering based on Jaccard similarity.

6. **Merge clusters.** To ensure that every pair of clusters are separable by conserved differentially expressed (DE) genes across all datasets, for each cluster, we first identified the top 3 nearest clusters. For each pair of such close-related clusters, we computed the differentially expressed genes using limma (Ritchie et al., 2015) in each dataset, and choose the DE genes that are significant in at least one dataset, while also having more than 2 folds change in the same direction in all datasets. We then compute the overall statistical significance based on such conserved DE genes for each dataset independently. If any of the dataset pass our DE gene criteria (Tasic et al., 2018), the pair of clusters remained separated, otherwise they were merged. DE genes were recomputed for merged clusters, and the process repeat until all clusters are separable by sufficient number of conserved DE genes. If one cluster has fewer than the minimal number of cells in a dataset, then this dataset is not used for DE gene computation for all pairs involving the given cluster. This step allows detection of unique clusters only present in a subset of clusters.

7. Repeat steps 1-6 for cells within cluster to gain finer resolution clusters until no clusters can be found.

8. Concatenate all the clusters from all the iterative clustering steps and perform final merging as described in step 6.

This integrative clustering pipeline allows us to resolve clusters at fine resolution, while ensuring proper alignment between datasets by requiring presence of conserved DE genes. It also allows us to leverage the strengths of different datasets. For example, between clusters that are separated by weakly expressed genes, SMART-Seq dataset provides the statistical power for separation, and the relevant genes help to separate 10X cells into clusters with consistent fold change. On the other hand, for clusters that have very few cells in SMART-Seq, 10X provides the statistical power for separation, and relevant genes are used to split SMART-Seq cells accordingly.

We applied this pipeline using both SMART-Seq and 10X datasets as reference, and the consensus clustering results were highly concordant with independent clustering results. All the major cell type markers are highly conserved at the cluster level. We calculated conserved DE genes between all pairs of clusters, and calculated the cluster means of these genes for each dataset. The concatenated cluster mean expression profiles across all datasets are used to build cell type taxonomy tree. Using the K nearest neighbors, we imputed the gene expression of SMART-seq cells based on 10X anchor genes, and imputed gene expression is used to create tSNE plot.

Confusion matrix analysis workflow—(a) Compute reference cluster medians: median gene expressions for each cell type (in this work) was computed for SMART-Seq cells and for 10X cells individually; (b) select a set of most important DE genes: a set of most important differentially expressed genes (~4570) was selected (this was done during clustering); (c) download target dataset for mapping: Gene expression and the cell types (clusters) of the target dataset (e.g., dataset from Cembrowski et al., 2018b) was downloaded; (d) choose the reference dataset: depending on the target data collection method, either SMART-Seq or 10X reference was chosen; (e) compute Pearson correlation: Pearson correlation was computed between each target cell gene expression and the cluster median gene expression of the reference dataset. A random selection of 80% of selected genes were used; (f) best mapped cell type was assigned: reference cell type which has the highest correlation with the target cell was assigned as the best mapped cell type for that cell; (g) step e and f were repeated 100 times: each time 80% of selected genes were used at random; (h) a probability matrix was built: using the result of step g, a probability matrix was built which shows what is the probability of a target cell to be mapped to each of the reference cell types; (i) cell type was assigned: for each target cell, the cell type which has the highest mapped probability was assigned as the corresponding cell type.

***In situ* hybridization (ISH) and anatomical mapping of the clusters—**ISH data used for anatomical registration and spatial validation of the transcriptional clusters are from Allen Mouse Brain Atlas (Lein et al., 2007), which is publicly available at https://portal.brain-map.org. Detailed description can be found at Allen Mouse Brain Atlas documentation page (http://help.brain-map.org/display/mousebrain/Documentation). Generally, 20-50 marker genes for each cluster were selected from transcriptome (e.g., Table S1) and their expression in Sub, PS and adjoining regions was examined and validated with Allen Mouse Brain Atlas ISH dataset. Afterward, representative ISH images for the locations of specific clusters were downloaded and displayed as shown in Figures 2, S1, and S3.

Selection of gene markers for Sub and PS—Since the “subicular” region distributes along a long DV axis, we chose the well-characterized dorsal portion for gene differentiation between Sub and PS. Based on unbiased transcriptomic clustering, we chose strongly and selectively expressed genes as marker genes for Sub and PS, respectively. For example, *Ntng2* and *Calbl* are strongly expressed in the region close to CA1 (i.e., away from PrS; see Figures 3 and S4) but not in the region close to PrS (i.e., away from CA1) and these two genes could be treated as PS markers based on the concept and definition of PS (Bienkowski et al., 2018; Ding, 2013; Lorente De No, 1934; Rosene and Van Hoesen, 1987; Saunders and Rosene, 1988; Saunders et al., 1988). Consistently, the genes expressed strongly and selectively in the region close to PrS but not in the region close to CA1 (e.g., *Nts* and *Bcl6)* were treated as Sub markers (see Figures 3 and S4). These selected gene markers were then applied to the whole “subicular” region along DV axis to obtain consistent and reliable boundaries of Sub and PS, which is critical for evaluation of tracer injections.

Animal surgery and tracer injection—The methods for animal surgery and tracer injection were reported previously (Oh et al., 2014) and can be found at the Allen Mouse

Brain Connectivity Atlas documentation page (http://help.brain-map.org//display/mouseconnectivity/Documentation). Briefly, both wild-type and Cre mice were anesthetized with 5% isoflurane and mounted onto a stereotaxic frame (model 1900; Kopf, Tujunga, CA) prior to surgery. During surgery, anesthesia was maintained at 1.8%−2% isoflurane. For subicular and prosubicular injections along the D-V axis, a glass pipette (inner tip diameter 10-20 mm) loaded with AAV was lowered to the desired depth based on the atlas of Paxinos and Franklin (2012). For wild-type mice, a pan-neuronal AAV vector expressing EGFP under the human synapsin I promoter (AAV2/1.pSynI.EGFP.WPRE.bGH) was injected in target regions, while in Cre driver mice a Cre-dependent AAV (AAV2/1.pCAG.-FLEX.EGFP.WPRE.bGH) was injected. The AAV (serotype 1, produced by UPenn viral core; titer > 10^{12} GC/ml) was delivered by iontophoresis (current 3 μΛ and 7 s on/7 s off duty cycle) for 5 minutes. After tracer injections, the skin incision was sutured and the mice were returned to their cages for recovery.

Brain preparation and imaging—After 21 days of survival time, mice were intracardially perfused with 10 ml 0.9% NaCl followed by 50 ml freshly prepared 4% paraformaldehyde (PFA) after anesthetization with 5% isoflurane. After extraction, brains were postfixed in 4% PFA at room temperature for 3-6 hours and overnight at 4 °C, then stored in PBS with 0.1% sodium azide. For imaging, brains were placed in 4.5% oxidized agarose (made by stirring 10 mM $NaIO_4$ in agarose), transferred to a phosphate buffer solution, and placed in a grid-lined embedding mold for standardized orientation in an aligned coordinate space. Multiphoton image acquisition was accomplished by using the TissueCyte 1000 system (TissueVision, Cambridge, MA) coupled with a Mai Tai HP DeepSee laser (Spectra Physics, Santa Clara, CA), as described in Oh et al. (2014) for the Allen Mouse Brain Connectivity Atlas.

Evaluation of tracer injection sites—Locations and extent of the injection sites in Sub and/or PS were evaluated based on the boundaries defined along DV axis of hippocampus in this study (see Figure 3). In addition, the term “effective injection site” was introduced in Cre-dependent viral tracing. Specifically, for example, when a tracer injection was involved in both region A and adjacent region B but the gene driving Cre was only expressed in cells of region A, then region A is the effective injection site because cells in region B would not express the GFP fluorescent tracer (see Table S2 for detailed Cre-lines and related effective injection sites).

QUANTIFICATION AND STATISTICAL ANALYSIS

Quantification of projection density was performed according to the methods and Informatics Data Processing Pipeline (IDP) for the Allen Mouse Brain Connectivity Atlas (Kuan et al., 2015; Oh et al., 2014). Briefly, an alignment module of the IDP was used to align all injection experiments with the average 3D model brain after image reprocessing. A signal algorithm, based on a combination of adaptive edge/line detection and morphological processing, was applied to each section image to differentiate positive fluorescent signal from background signal. Segmented signal pixels were counted as projection strength in the claustrum and cortical areas. It should be noted that the detection algorithm operates on a per-image basis and that passing fibers and axon terminals were not distinguished (see e.g.,

Figure S9). Imperfect alignment of each injection image set with the Allen Mouse Brain CCF may also affect the quantification of the projections.

Supplementary Material

Refer to Web version on PubMed Central for supplementary material.

ACKNOWLEDGMENTS

We are grateful for the technical support and expertise of the many staff members in the Allen Institute who are not part of the authorship of this paper. This work was funded by the Allen Institute for Brain Science. The authors wish to thank the Allen Institute founders, Paul G. Allen and Jody Allen, for their vision, encouragement, and support. The research was also supported by BRAIN Initiative Cell Census Network (BICCN) grant award U19MH114830 from the National Institute of Mental Health to H.Z. The content issolelythe responsibility of the authors and does not necessarily represent the official views of the National Institute of Health and National Institute of Mental Health.

REFERENCES

Aggleton JP (2012). Multiple anatomical systems embedded within the primate medial temporal lobe: implications for hippocampal function. Neurosci. Biobehav. Rev 36, 1579–1596. [PubMed: 21964564]

Aggleton JP, and Christiansen K (2015). The subiculum: the heart of the extended hippocampal system. Prog. Brain Res 219, 65–82. [PubMed: 26072234]

Andrzejewski ME, Spencer RC, and Kelley AE (2006). Dissociating ventral and dorsal subicular dopamine D1 receptor involvement in instrumental learning, spontaneous motor behavior, and motivation. Behav. Neurosci 120, 542–553. [PubMed: 16768606]

Aqrabawi AJ, Browne CJ, Dargaei Z, Garand D, Khademullah CS, Woodin MA, and Kim JC (2016). Top-down modulation of olfactory-guided behaviours by the anterior olfactory nucleus pars medialis and ventral hippocampus. Nat. Commun 7, 13721. [PubMed: 28004701]

Arikuni T, Sako H, and Murata A (1994). Ipsilateral connections of the anterior cingulate cortex with the frontal and medial temporal cortices in the macaque monkey. Neurosci. Res 21, 19–39. [PubMed: 7535904]

Barbas H, and Blatt GJ (1995). Topographically specific hippocampal projections target functionally distinct prefrontal areas in the rhesus monkey. Hippocampus 5, 511–533. [PubMed: 8646279]

Bienkowski MS, Bowman I, Song MY, Gou L,Ard T, Cotter K, Zhu M, Benavidez NL, Yamashita S, Abu-Jaber J, et al. (2018). Integration ofgene expression and brain-wide connectivity reveals the multiscale organization of mouse hippocampal networks. Nat. Neurosci 21, 1628–1643. [PubMed: 30297807]

Butler A, Hoffman P, Smibert P, Papalexi E, and Satija R (2018). Integrating single-cell transcriptomic data across different conditions, technologies, and species. Nat. Biotechnol 36, 411–420. [PubMed: 29608179]

Canteras NS, and Swanson LW (1992). Projections of the ventral subiculum to the amygdala, septum, and hypothalamus: a PHAL anterograde tract-tracing study in the rat. J. Comp. Neurol 324, 180–194. [PubMed: 1430328]

Cassel JC, Pereira de Vasconcelos A, Loureiro M, Cholvin T, Dalrymple-Alford JC, and Vertes RP (2013). The reuniens and rhomboid nuclei: neuro-anatomy, electrophysiological characteristics and behavioral implications. Prog. Neurobiol 111, 34–52. [PubMed: 24025745]

Cembrowski MS, Phillips MG, DiLisio SF, Shields BC, Winnubst J, Chandrashekar J, Bas E, and Spruston N (2018a). Dissociable structural and functional hippocampal outputs via distinct subiculum cell classes. Cell 173, 1280–1292.e18. [PubMed: 29681453]

Cembrowski MS, Wang L, Lemire AL, Copeland M, DiLisio SF, Clements J, and Spruston N (2018b). The subiculum is a patchwork of discrete subregions. eLife 7, e37701. [PubMed: 30375971]

Cenquizca LA, and Swanson LW (2007). Spatial organization ofdirect hippocampal field CA1 axonal projectionstothe rest of the cerebral cortex. Brain Res. Brain Res. Rev 56, 1–26.

Christensen MK, and Frederickson CJ (1998). Zinc-containing afferent projections to the rat corticomedial amygdaloid complex: a retrograde tracing study. J. Comp. Neurol 400, 375–390. [PubMed: 9779942]

Christiansen K, Dillingham CM, Wright NF, Saunders RC, Vann SD, and Aggleton JP (2016). Complementary subicular pathways to the anterior thalamic nuclei and mammillary bodies in the rat and macaque monkey brain. Eur. J. Neurosci 43, 1044–1061. [PubMed: 26855336]

Christie MJ, Summers RJ, Stephenson JA, Cook CJ, and Beart PM (1987). Excitatory amino acid projections to the nucleus accumbens septi in the rat: a retrograde transport study utilizing D[3H]aspartate and [3H]GABA. Neuroscience 22, 425–439. [PubMed: 2823173]

Coras R, Pauli E, Li J, Schwarz M, Rossler K, Buchfelder M, Hamer H, Stefan H, and Blumcke I (2014). Differential influence of hippocampal subfields to memory formation: insights from patients with temporal lobe epilepsy. Brain 137, 1945–1957. [PubMed: 24817139]

Cullinan WE, Herman JP, and Watson SJ (1993). Ventral subicular interaction with the hypothalamic paraventricular nucleus: evidence for a relay in the bed nucleus of the stria terminalis. J. Comp. Neurol 332, 1–20. [PubMed: 7685778]

Daigle TL, Madisen L, Hage TA, Valley MT, Knoblich U, Larsen RS, Takeno MM, Huang L, Gu H, Larsen R, et al. (2018).ASuite of Transgenic Driver and Reporter Mouse Lines with Enhanced Brain-Cell-Type Targeting and Functionality. Cell 174, 465–480.e22. [PubMed: 30007418]

Ding SL (2013). Comparative anatomy of the prosubiculum, subiculum, pre-subiculum, postsubiculum, and parasubiculum in human, monkey, and rodent. J. Comp. Neurol 521, 4145–4162. [PubMed: 23839777]

Ding SL, and Van Hoesen GW (2015). Organization and detailed parcellation of human hippocampal head and body regions based on a combined analysis of cyto- and chemoarchitecture. J. Comp. Neurol 523, 2233–2253. [PubMed: 25872498]

Ding SL, Royall JJ, Sunkin SM, Ng L, Facer BA, Lesnar P, Guillozet-Bongaarts A, McMurray B, Szafer A, Dolbeare TA, et al. (2016). Comprehensive cellular-resolution atlas of the adult human brain. J. Comp. Neurol 524, 3127–3481. [PubMed: 27418273]

Doan TP, Lagartos-Donate MJ, Nilssen ES, Ohara S, and Witter MP (2019). Convergent projections from perirhinal and postrhinal cortices suggest a multisensory nature of lateral, but Not medial, entorhinal cortex. Cell Rep. 29, 617–627.e7. [PubMed: 31618631]

Farrell MR, Sayed JA, Underwood AR, and Wellman CL (2010). Lesion of infralimbic cortex occludes stress effects on retrieval of extinction but not fear conditioning. Neurobiol. Learn. Mem 94, 240–246. [PubMed: 20538067]

Fudge JL, deCampo DM, and Becoats KT (2012). Revisiting the hippocampal-amygdala pathway in primates: association with immature-appearing neurons. Neuroscience 212, 104–119. [PubMed: 22521814]

Godsil BP, Kiss JP, Spedding M, and Jay TM (2013). The hippocampal-prefrontal pathway: the weak link in psychiatric disorders? Eur. Neuropsychopharmacol 23, 1165–1181. [PubMed: 23332457]

Hafting T, Fyhn M, Molden S, Moser MB, and Moser EI (2005). Micro-structure of a spatial map in the entorhinal cortex. Nature 436, 801–806. [PubMed: 15965463]

Harris JA, Hirokawa KE, Sorensen SA, Gu H, Mills M, Ng LL, Bohn P, Mortrud M, Ouellette B, Kidney J, et al. (2014). Anatomical characterization of Cre driver mice for neural circuit mapping and manipulation. Front. Neural Circuits 8, 76. [PubMed: 25071457]

Herman JP, and Mueller NK (2006). Role ofthe ventral subiculum in stress integration. Behav. Brain Res 174, 215–224. [PubMed: 16876265]

Honda Y, and Ishizuka N (2015). Topographic distribution of cortical projection cells in the rat subiculum. Neurosci. Res 92, 1–20. [PubMed: 25514386]

Howell GA, Perez-Clausell J, and Frederickson CJ (1991). Zinc containing projections to the bed nucleus of the stria terminalis. Brain Res. 562,181–189. [PubMed: 1773336]

Hsu DT, Kirouac GJ, Zubieta JK, and Bhatnagar S (2014). Contributions of the paraventricular thalamic nucleus in the regulation of stress, motivation, and mood. Front. Behav. Neurosci 8, 73. [PubMed: 24653686]

Huang LW, Simonnet J, Nassar M, Richevaux L, Lofredi R, and Fricker D (2017). Laminar localization and projection-specific properties of presubicular neurons targeting the lateral mammillary nucleus, thalamus, or medial entorhinal cortex. eNeuro 4, ENEURO.0370–16.2017.

Hutter JA, Martel A, Trigiani L, Barrett SG, and Chapman CA (2013). Rewarding stimulation of the lateral hypothalamus induces a dopamine-dependent suppression of synaptic responses in the entorhinal cortex. Behav. Brain Res 252, 266–274. [PubMed: 23747609]

Ishizuka N (2001). Laminar organization of the pyramidal cell layer ofthe subiculum in the rat. J. Comp. Neurol 435, 89–110. [PubMed: 11370013]

Jankowski MM, Islam MN, Wright NF, Vann SD, Erichsen JT, Aggleton JP, and O'Mara SM (2014). Nucleus reuniens of the thalamus contains head direction cells. eLife 3.

Jay TM, Glowinski J, and Thierry AM (1989). Selectivity of the hippocampal projection to the prelimbic area of the prefrontal cortex in the rat. Brain Res. 505, 337–340. [PubMed: 2598054]

Jimenez JC, Su K, Goldberg AR, Luna VM, Biane JS, Ordek G, Zhou P, Ong SK, Wright MA, Zweifel L, et al. (2018). Anxiety cells in a hippocampal-hypothalamic circuit. Neuron 97, 670–683.e6. [PubMed: 29397273]

Jin J, and Maren S (2015). Fear renewal preferentially activates ventral hippocampal neurons projecting to both amygdala and prefrontal cortex in rats. Sci. Rep 5, 8388. [PubMed: 25669753]

Kishi T, Tsumori T, Yokota S, and Yasui Y (2006). Topographical projection from the hippocampal formation to the amygdala: a combined anterograde and retrograde tracing study in the rat. J. Comp. Neurol 496, 349–368. [PubMed: 16566004]

Kuan L, Li Y, Lau C, Feng D, Bernard A, Sunkin SM, Zeng H, Dang C, Hawrylycz M, and Ng L (2015). Neuroinformatics of the Allen Mouse Brain Connectivity Atlas. Methods 73, 4–17. [PubMed: 25536338]

Leal SL, Noche JA, Murray EA, and Yassa MA (2017). Disruption of amygdala-entorhinal-hippocampal network in late-life depression. Hippocampus 27, 464–476. [PubMed: 28085210]

Lein ES, Hawrylycz MJ, Ao N, Ayres M, Bensinger A, Bernard A, Boe AF, Boguski MS, Brockway KS, Byrnes EJ, et al. (2007). Genome-wide atlas of gene expression in the adult mouse brain. Nature 445, 168–176. [PubMed: 17151600]

Lever C, Burton S, Jeewajee A, O'Keefe J, and Burgess N (2009). Boundary vector cells in the subiculum of the hippocampal formation. J. Neurosci 29, 9771–9777. [PubMed: 19657030]

Lopez R, Regier J, Cole MB, Jordan MI, and Yosef N (2018). Deep generative modeling for single-cell transcriptomics. Nat. Methods 15, 1053–1058. [PubMed: 30504886]

Lorente De No R (1934). Studies on the structure of the cerebral cortex. II. Continuation of the study of the ammonic system. J. Psychol. Neurol 46, 113–177.

Lu W, Chen S, Chen X, Hu J, Xuan A, and Ding SL (2020). Localization of area prostriata and its connections with primary visual cortex in rodent. J. Comp. Neurol 528, 389–406. [PubMed: 31423581]

Mannella F, Gurney K, and Baldassarre G (2013). The nucleus accumbens as a nexus between values and goals in goal-directed behavior: a review and a new hypothesis. Front. Behav. Neurosci 7, 135. [PubMed: 24167476]

McDonald AJ (1998). Cortical pathways to the mammalian amygdala. Prog. Neurobiol 55, 257–332. [PubMed: 9643556]

McGinnis CS, Murrow LM, and Gartner ZJ (2019). DoubletFinder: doublet detection in single-cell RNA sequencing data using artificial nearest neighbors. Cell Syst. 8, 329–337.e4. [PubMed: 30954475]

Meibach RC, and Siegel A (1977a). Efferent connections of the hippocampal formation in the rat. Brain Res. 124, 197–224. [PubMed: 402984]

Meibach RC, and Siegel A (1977b). Thalamic projections of the hippocampal formation: evidence for an alternate pathway involving the internal capsule. Brain Res. 134, 1–12. [PubMed: 410479]

Naber PA, and Witter MP (1998). Subicular efferents are organized mostly as parallel projections: a double-labeling, retrograde-tracing study in the rat. J. Comp. Neurol 393, 284–297. [PubMed: 9548550]

O'Mara SM, Sanchez-Vives MV, Brotons-Mas JR, and O'Hare E (2009). Roles for the subiculum in spatial information processing, memory, motivation and the temporal control of behaviour. Prog. Neuropsychopharmacol. Biol. Psychiatry 33, 782–790. [PubMed: 19393282]

Oh SW, Harris JA, Ng L, Winslow B, Cain N, Mihalas S, Wang Q, Lau C, Kuan L, Henry AM, et al. (2014). A mesoscale connectome of the mouse brain. Nature 508, 207–214. [PubMed: 24695228]

Olson JM, Tongprasearth K, and Nitz DA (2017). Subiculum neurons map the current axis of travel. Nat. Neurosci 20, 170–172. [PubMed: 27991899]

Ottersen OP (1982). Connections of the amygdala of the rat. IV: Corticoa-mygdaloid and intraamygdaloid connections as studied with axonal transport of horseradish peroxidase. J. Comp. Neurol 205, 30–48. [PubMed: 7068948]

Parfitt GM, Nguyen R, Bang JY, Aqrabawi AJ, Tran MM, Seo DK, Richards BA, and Kim JC (2017). Bidirectional control of anxiety-related behaviors in mice: role of inputs arising from the ventral hippocampus to the lateral septum and medial prefrontal cortex. Neuropsychopharmacology 42, 1715–1728. [PubMed: 28294135]

Paxinos G, and Franklin KBJ (2012). The Mouse Brain in Stereotaxic Coordinates (Elsevier Academic Press).

Phillipson OT, and Griffiths AC (1985). The topographic order of inputs to nucleus accumbens in the rat. Neuroscience 16, 275–296. [PubMed: 4080159]

Potvin O, Allen K, Thibaudeau G, Dore FY, and Goulet S (2006). Performance on spatial working memory tasks after dorsal or ventral hippocampal lesions and adjacent damage to the subiculum. Behav. Neurosci 120, 413–422. [PubMed: 16719705]

Preston-Ferrer P, Coletta S, Frey M, and Burgalossi A (2016). Anatomical organization of presubicular head-direction circuits. eLife 5, e14592. [PubMed: 27282390]

Riaz S, Schumacher A, Sivagurunathan S, Van Der Meer M, and Ito R (2017). Ventral, but not dorsal, hippocampus inactivation impairs reward memory expression and retrieval in contexts defined by proximal cues. Hippocampus 27, 822–836. [PubMed: 28449268]

Ritchie ME, Phipson B, Wu D, Hu Y, Law CW, Shi W, and Smyth GK (2015). limma powers differential expression analyses for RNA-sequencing and microarray studies. Nucleic Acids Res. 43, e47. [PubMed: 25605792]

Roy DS, Kitamura T, Okuyama T, Ogawa SK, Sun C, Obata Y,Yoshiki A, and Tonegawa S (2017). Distinct neural circuits for the formation and retrieval of episodic memories. Cell 170, 1000–1012.e19. [PubMed: 28823555]

Saunders RC, and Rosene DL (1988). A comparison ofthe efferents ofthe amygdala and the hippocampal formation in the rhesus monkey: I. Convergence in the entorhinal, prorhinal, and perirhinal cortices. J. Comp. Neurol 271, 153–184. [PubMed: 2454246]

Saunders RC, Rosene DL, and Van Hoesen GW (1988). Comparison of the efferents of the amygdala and the hippocampal formation in the rhesus monkey: II. Reciprocal and non-reciprocal connections. J. Comp. Neurol 271, 185–207. [PubMed: 2454247]

Shi CJ, and Cassell MD (1999). Perirhinal cortex projections to the amygdaloid complex and hippocampal formation in the rat. J. Comp. Neurol 406, 299–328. [PubMed: 10102498]

Strange BA, Witter MP, Lein ES, and Moser EI (2014). Functional organization of the hippocampal longitudinal axis. Nat. Rev. Neurosci 15,655–669. [PubMed: 25234264]

Subhadeep D, Srikumar BN, Shankaranarayana Rao BS, and Kutty BM (2017). Exposureto short photoperiod regime reducesventral subicular lesion-induced anxiety-like behavior in Wistar rats. Physiol. Behav 170, 124–132. [PubMed: 28017681]

Swanson LW, and Cowan WM (1977). An autoradiographic study ofthe organization ofthe efferent connections ofthe hippocampal formation in the rat. J. Comp. Neurol 172, 49–84. [PubMed: 65364]

Sweeney P, and Yang Y (2015). An excitatory ventral hippocampusto lateral septum circuit that suppresses feeding. Nat. Commun 6, 10188. [PubMed: 26666960]

Sweeney P, and Yang Y (2016). An inhibitory septum to lateral hypothalamus circuit that suppresses feeding. J. Neurosci 36, 11185–11195. [PubMed: 27807162]

Tang Q, Burgalossi A, Ebbesen CL, Sanguinetti-Scheck JI, Schmidt H, Tukker JJ, Naumann R, Ray S, Preston-Ferrer P, Schmitz D, and Brecht M (2016). Functional architecture of the rat parasubiculum. J. Neurosci 36, 2289–2301. [PubMed: 26888938]

Tasic B, Yao Z, Graybuck LT, Smith KA, Nguyen TN, Bertagnolli D, Goldy J, Garren E, Economo MN, Viswanathan S, et al. (2018). Shared and distinct transcriptomic cell types across neocortical areas. Nature 563, 72–78. [PubMed: 30382198]

Taube JS (2007). The head direction signal: origins and sensory-motor integration. Annu. Rev. Neurosci 30, 181–207. [PubMed: 17341158]

Van Hoesen GW, and Hyman BT (1990). Hippocampal formation: anatomy and the patterns of pathology in Alzheimer's disease. Prog. Brain Res 83, 445–457. [PubMed: 2392569]

van Strien NM, Cappaert NL, and Witter MP (2009). The anatomy of memory: an interactive overview of the parahippocampal-hippocampal network. Nat. Rev. Neurosci 10, 272–282. [PubMed: 19300446]

Veening JG (1978). Cortical afferents of the amygdaloid complex in the rat: an HRP study. Neurosci. Lett 8, 191–195. [PubMed: 19605157]

Vranjkovic O, Pina M, Kash TL, and Winder DG (2017). The bed nucleus of the stria terminalis in drug-associated behavior and affect: A circuit-based perspective. Neuropharmacology 122, 100–106. [PubMed: 28351600]

Wang J, and Barbas H (2018). Specificity of primate amygdalar pathways to hippocampus. J. Neurosci 38, 10019–10041. [PubMed: 30249799]

Wang Q, Ding S-L, Li Y, Royall J, Feng D, Lesnar P, Graddis N, Naeemi M, Facer B, Ho A, et al. (2020). The Allen Mouse Brain Common Coordinate Framework: A 3D Reference Atlas. Cell. 10.1016/j.cell.2020.04.007.

Wassum KM, and Izquierdo A (2015). The basolateral amygdala in reward learning and addiction. Neurosci. Biobehav. Rev 57, 271–283. [PubMed: 26341938]

Weller KL, and Smith DA (1982). Afferent connectionstothe bed nucleusof the stria terminalis. Brain Res. 232, 255–270. [PubMed: 7188024]

Witter MP (2006). Connections of the subiculum of the rat: topography in relation to columnar and laminar organization. Behav. Brain Res 174, 251–264. [PubMed: 16876886]

Witter MP, Ostendorf RH, and Groenewegen HJ (1990). Heterogeneity in the dorsal subiculum of the rat. distinct neuronal zones project to different cortical and subcortical targets. Eur. J. Neurosci 2, 718–725. [PubMed: 12106290]

Wyss JM, and Van Groen T (1992). Connections between the retrosplenial cortex and the hippocampal formation in the rat: a review. Hippocampus 2, 1–11. [PubMed: 1308170]

Yukie M (2000). Connections between the medial temporal cortex and the CA1 subfield of the hippocampal formation in the Japanese monkey (Macaca fuscata). J. Comp. Neurol 423, 282–298. [PubMed: 10867659]

Highlights

- Twenty-seven transcriptomic cell types and their spatial locations identified in subicular region
- Distinct cell types and circuits of the subiculum (Sub) and prosubiculum (PS) identified
- Anatomical borders and dorsoventral extent of the Sub and PS comprehensively determined
- Brain-wide cell-type-specific projections of the Sub and PS revealed with Cre lines

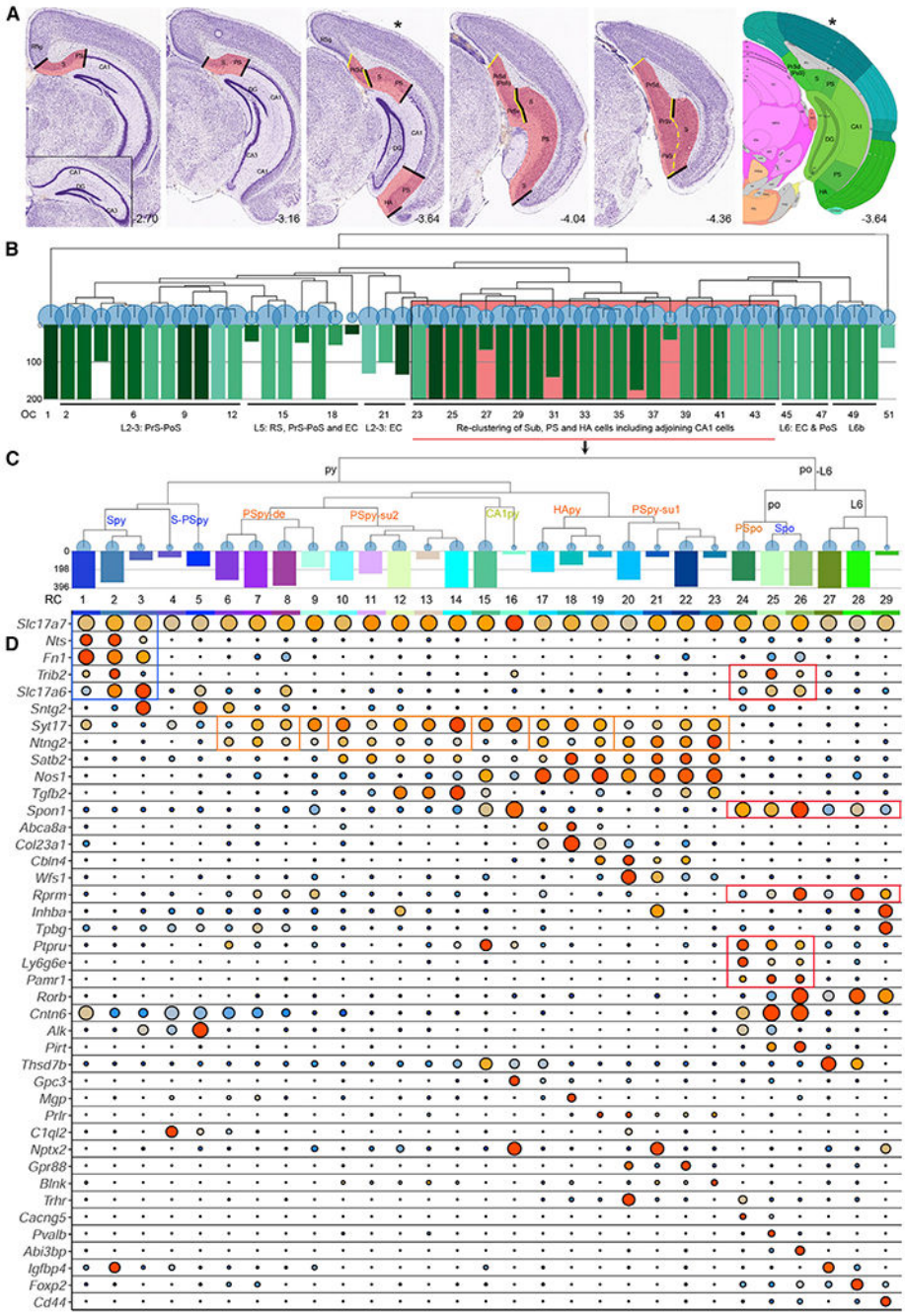

Figure 1. Transcriptomic Classification of Sub and PS Cell Types

(A) Microdissection of tissue from the Sub-PS-HA (region between black bars), PrS-PoS-PaS (between yellow bars), orall subicular complex (all highlighted area) in sequential coronal sections. The inset in the first image shows the lack of the Sub-PS at more anterior levels. The last image shows the reference atlas plate for the Sub-PS-HA region that matches the third image (*). Bregma levels are indicated at the bottom of each panel.

(B) Hierarchical clustering of cells from the subicular complex (10X). OC1-OC51 indicate original clusters (OCs). Highlighted OC23-OC44 were re-clustered in (C).

(C) Hierarchical re-clustering (RC) of cells from the Sub-PS-HA region (i.e., cells from OC23-OC44 in B). RC1-RC29 indicate the cluster numbers from RC.
(D) Dot plot of selected gene markers (from 10X data) from RC (see Table S1). Color of the dots indicates cluster mean expression (log scale), normalized by row (blue to red: 0–1). Size of the dots indicates percentage of cells with CPM (counts per million) > 1. Major clusters and marker genes are outlined with colored boxes. For abbreviations, see STAR Methods.
See also Figures S1, S2, S3, and S10; Table S1.

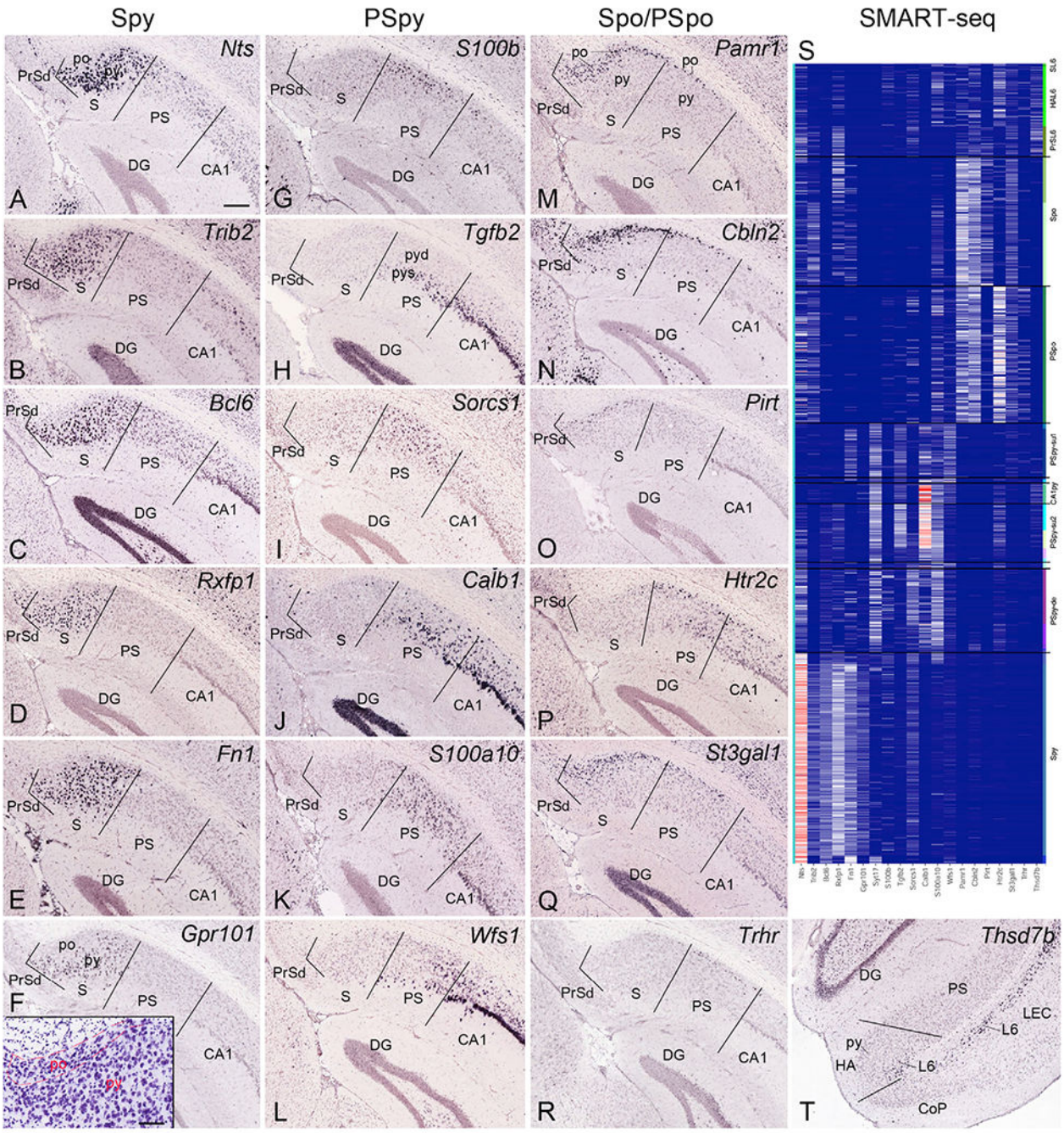

Figure 2. Major Transcriptomic Clusters Mapped to Anatomic Regions

Black lines mark the areal borders in each panel. Gene markers are indicated on each panel (A-R and T).

(A–F) Marker genes selectively expressed in the Spy with fewor no expressed cells in the PSpy. The inset in (F) showsthe cell shape and size difference between the py and po.

(G–L) Marker genes selectively expressed in the PSpy with few or no expressed cells in the Spy.

(M–R) Marker genes selectively expressed in the Spo and/or PSpo with few or no expressed cells in the Spy and PSpy.
(S) Corresponding transcriptomic clusters revealed with SMART-seq, which are largely consistent with the results from 10X in Figure 1D.
(T) Thsd7b expression in layer 6 (L6) of the HA and EC.
Scale bars: 210 μm (A–R and T); 95 μm in the inset in (F). See also Figures S1 and S3; Table S1.

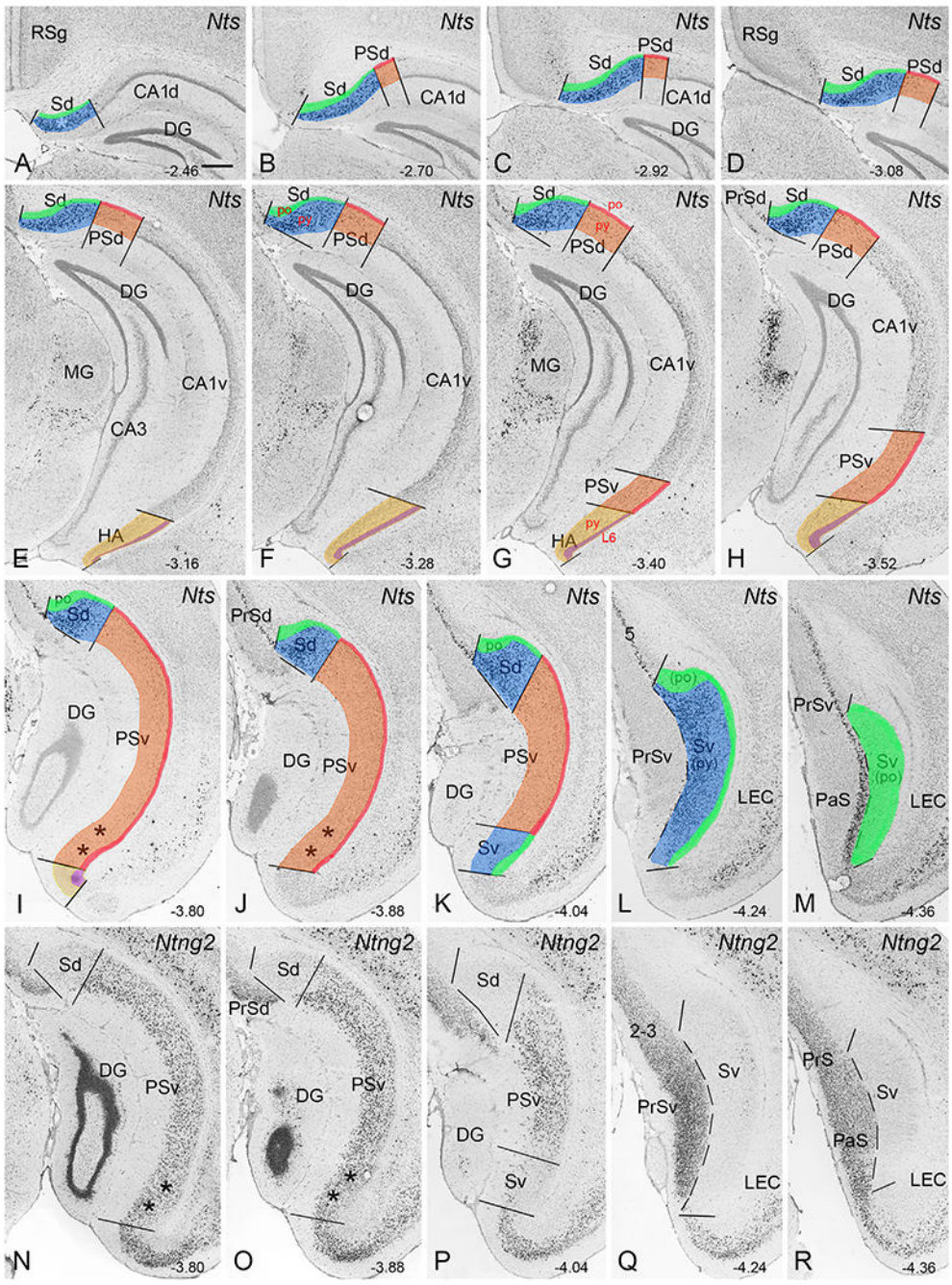

Figure 3. Borders, Extent, and Topography of the Dorsal and Ventral Sub and PS

(A–M) Borders, extent, and topography ofthe dorsal and ventral Sub and PS on *Nts* sequential rostral (A)-caudal (M) coronal ISH sections. *Nts* is predominantly expressed in the pyramidal layer (py) of the Sd (A–K) and Sv (L) with few or no expressed cells in the PSd and PSv or the polymorphic layer(po) of the Sd and Sv.

(N–R) Borders, extent, and topography of the ventral Sub and PS on *Ntng2* sequential coronal ISH sections. *Ntng2* is predominantly expressed in the PS. Note that the PSv is easily distinguishable from the Sv.

The most dorsal part (* in A) contains only the Sub, while the most ventral part (** in I, J, N, and O) contains only the PS (this finding is obviously observed in sequential sagittal sections shown in Figure S4). Note also that the color-coded po of the Sub and PS in (A)–(M) contains cells from deeper layers L6-L6b (for the Sub) or L6b (forthe PS) for concise illustration. Bregma levels are indicated at the bottom of each panel. Scale bar: 350 mm. See also Figures S4 and S10.

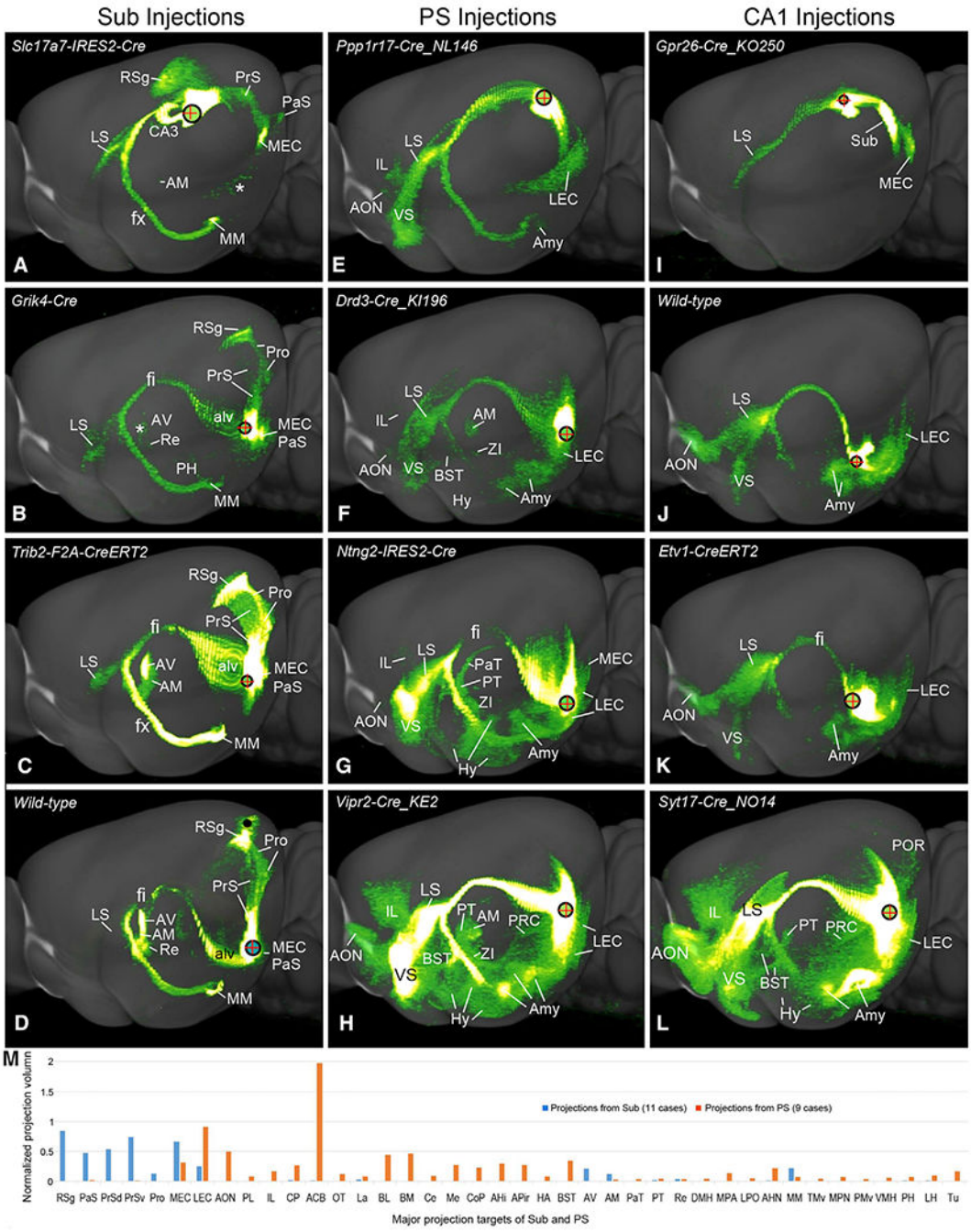

Figure 4. Comparison of Overall Projection Patterns of the Sub, PS, and CA1

Detected fluorescent signals in each case were projected onto the lateral view of the Allen Mouse CCF template. The black circle with a red cross indicates the injection site.

(A–D) Projection patterns of the dorsal (A) and ventral (B-D, for different mice indicated) Sub in four representative cases. Axon terminal projections to the RSg, PrS, PaS, MEC, AV, and MM areobserved in all Sub cases. Note the dorsal injection (A) also includes part of the underlying DG, which results in terminal labeling in CA3. Some retrogradely labeled

neurons were present occasionally in the LEC and AV (white asterisks in A and B). The black dot in (D) indicates some injection contamination in V1.

(E–H) Projection patterns of the dorsal (E) and ventral (F-H, fordifferent mice indicated) PS in four representative cases. Axon terminal projections to the LEC, IL, VS, amygdala, and AON are seen in all PS cases, while those to the BST and hypothalamus (Hy) are found in all PSv cases.

(I–L) Projection patterns of the dorsal (I) and ventral (J-L, for different mice indicated) CA1 in four representative cases. In general, CA1 shows somewhat similar projection patterns to the PS but not to the Sub.

(M) Quantitative comparison of the Sub (blue bars) and PS (orange bars) projections.

See also Figures S5, S6, S7, and S8; Table S2.

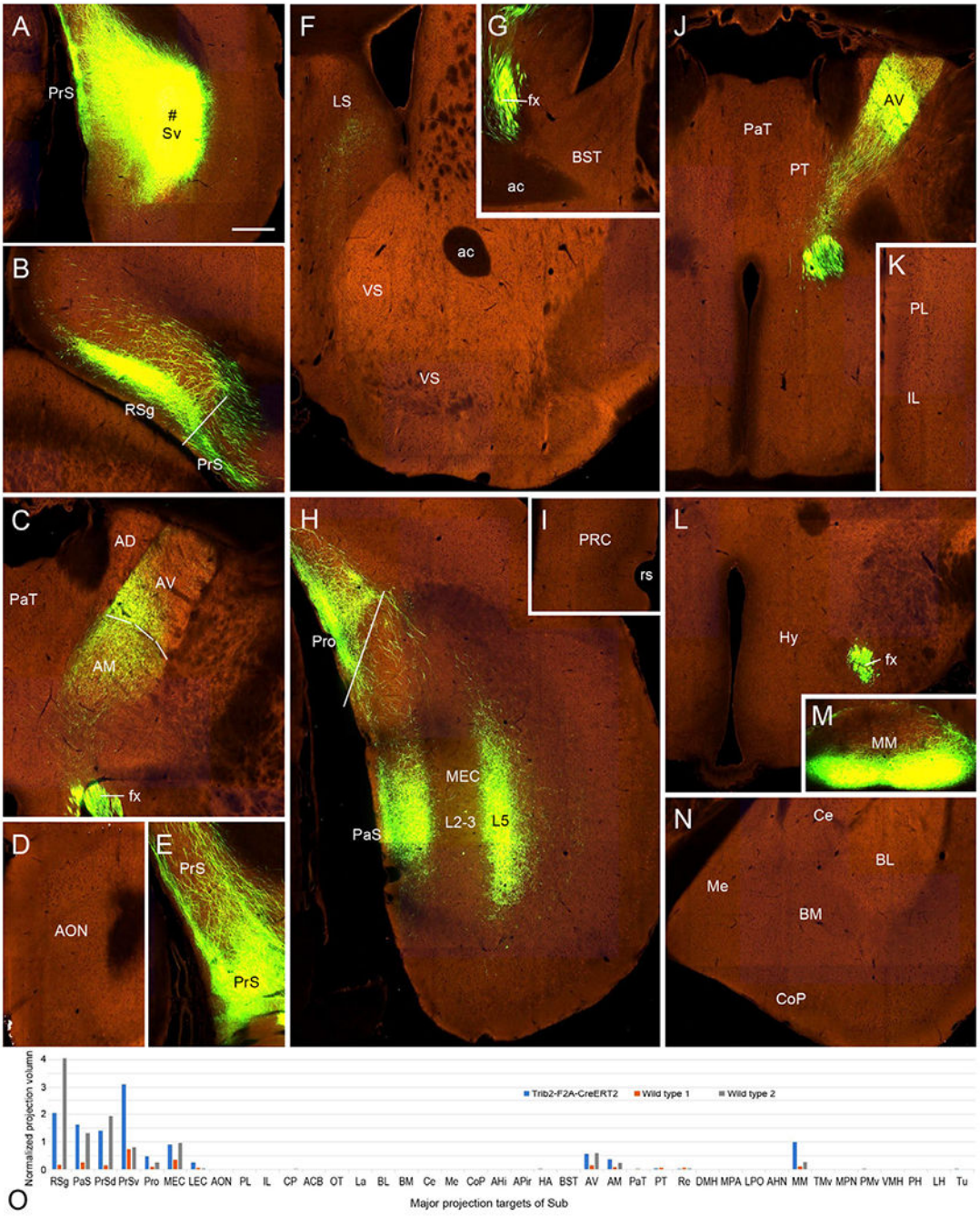

Figure 5. Limited Efferent Projections from the Ventral Sub

A *Trib2*-F2A-CreERT2 mouse is used as a representative case (overview in Figure 4C).

(A) The rAAV injection site (# marks the center) lies in the ventral Sub, marked by the Sv in Figures 3L and 3Q.

(B) Terminal labeling in L2/3 of the RSg.

(C) Terminal labeling in the middle AV and AM but not in the AD.

(D) Absence of terminal labeling in the AON.

(E) Fiber labeling in the dorsal PrS (the fibers pass through the PrS to the RSg) and strong terminal labeling in the ventral PrS.
(F) Terminal labeling in the LS with no labeling in the VS.
(G) Absence of labeling in the BST.
(H) Terminal labeling in the area prostriata (Pro), ventral PaS, and ventromedial MEC (mostly in L5).
(I) Absence of labeling in the PRC.
(J) Terminal labeling in the anterior AV with no labeling in the PaT, PT, and supraoptic hypothalamic regions.
(K) Absence of labeling in the PL and IL.
(L) Absence of labeling in the tuberal region (DMH and VMH) of the hypothalamus.
(M) Terminal labeling in the ventral portion of the MM.
(N) Absence of labeling in the amygdala.
(O) Quantitative comparison of Sub projections in this case (*Trib2*-F2A-CreERT2, blue bars) and in two WT cases (WT 1 and 2, orange and gray bars). Scale bar: 280 μm (A-N). See also Figures S5, S6, and S7; Table S2.

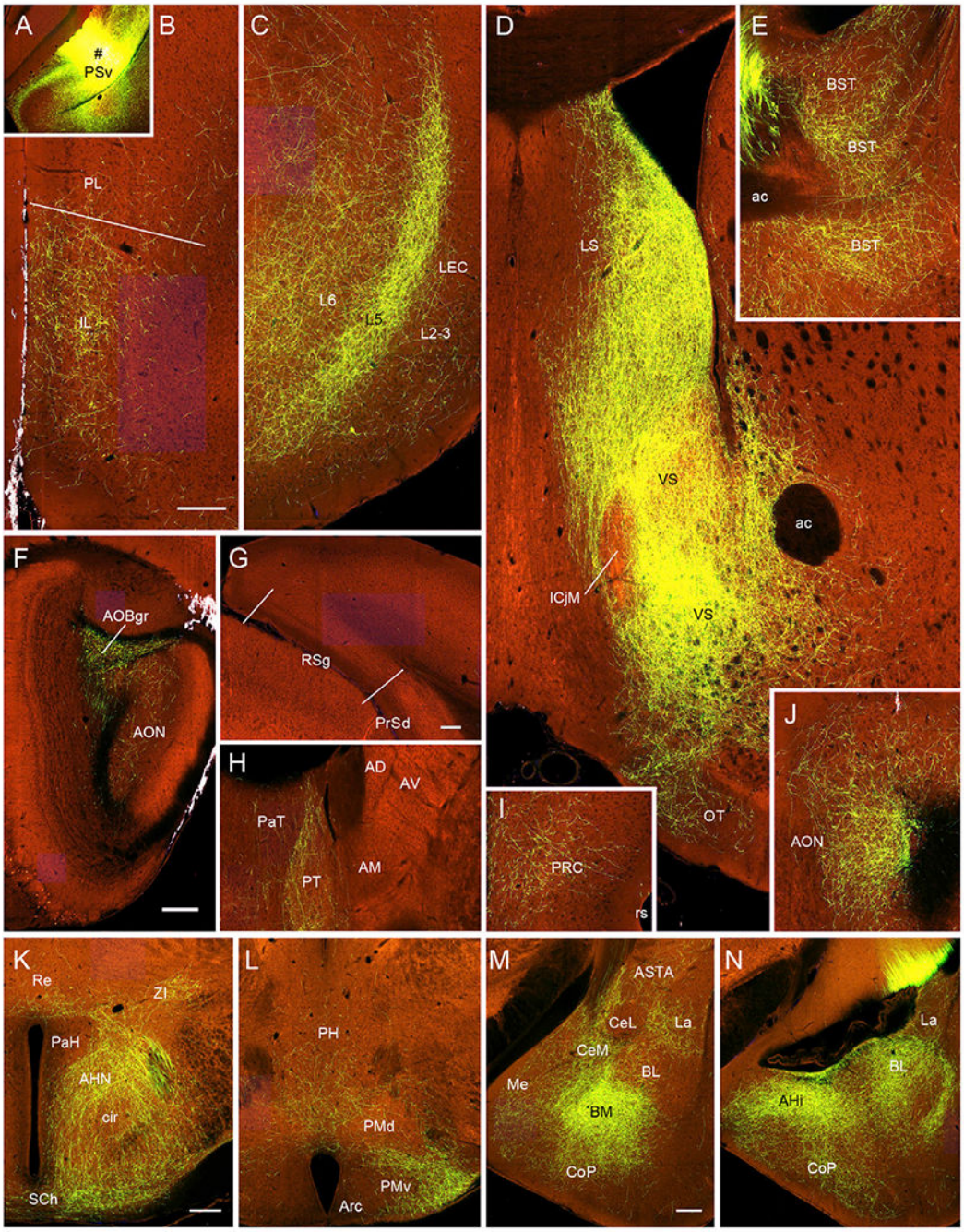

Figure 6. Widespread Efferent Projections from the Ventral PS

(A) A rAAV injection site (# marks the center) of a *Syt17*-Cre_NO14 mouse lies in the most ventral PS, marked by ** in Figures 3I and 3N.

(B–N) Axon terminal labeling in the PL, IL (B), LEC (C), LS, VS (D), BST (E), AOB (F) (mainly in its granular layer, AOBgr), RSg, PrSd (G) (no labeling), PT (H), PRC (I), AON (J), Re, ZI, AHN, SCh (K), ventral PH, lateral PMv (L), La, anterior BL, BM, Me, CeM, ASTA (M), AHi, posterior BL, and CoP(N). Note much less labeling on the major island of Island of Calleja (ICjM) (D), PaT (H), PaH (K), PMd (L), and CeL (M). Note also the

absence of labeling in the AM (H). Overall distribution pattern of labeled terminals in this case is similar to that in *Vipr2*-Cre_KE2 shown in Figure 4H, except for strong AM labeling in the latter.

Scale bars: 200 μm (B-E, I, and J); 280 μm (F and H); 140 μm (G); 200 μm (K and L); 200 μm (M and N). See also Figure S8; Table S2.

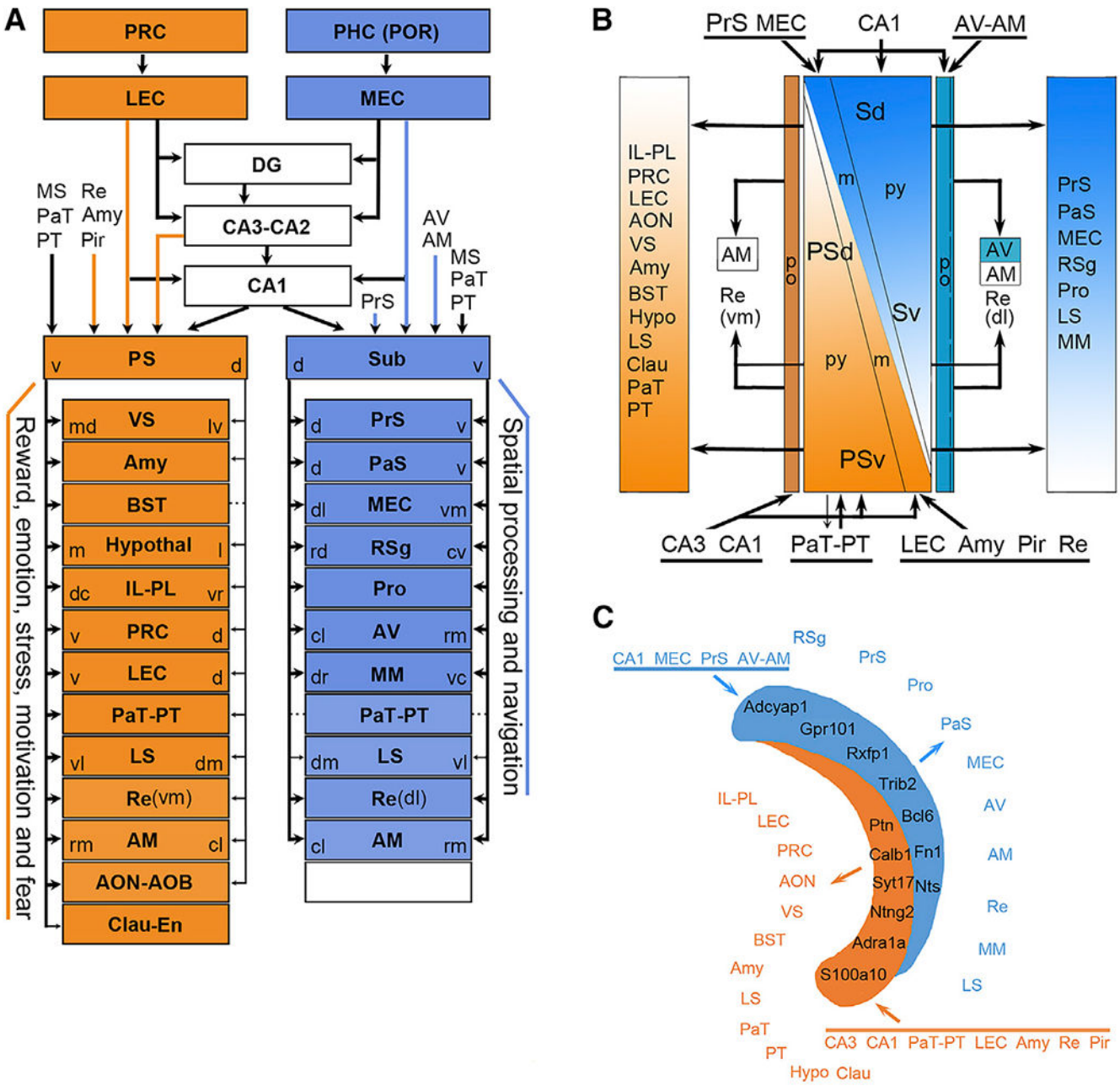

Figure 7. Summary of Distinct Circuits and Transcriptomic Cell Types of the Sub and PS

(A) Differential inputs and outputs of the Sub and PS in the context of the entire hippocampal circuit. The Sub mostly projects to regions important for spatial processing and navigation, while the PS mostly projects to widespread brain regions critical for reward, emotion, stress, motivation, anxiety, and fear. Note that the PS but not the Sub projections show obvious DV differences and that both the PS and the Sub display topographic projections to most of their targets. Potential convergence of Sub and PS projections may exist in the AM, RE, MM and LS. The Hypothal indicates most of the hypothalamic regions, including the MM. Clau-En, claustrum and endopiriform nucleus.

(B) Laminar organization of the inputs and outputs of the Sub and PS with relation to cell types. The PrS and MEC project to the molecular layer (m), while the AV-AM of the anterior thalamus projects to the polymorphic layer (po) of the Sub. CA1 projects to all layers of the Sub. In the PS, inputs from the LEC, amygdala, Pir, and Re mainly project to the molecular layer, while those from the PaT-PT of the thalamus mainly innervate the pyramidal layer (py). Inputs from hippocampal CA3 and CA1 project to all layers. As for outputs, the polymorphic layer of the Sub and PS projects to differential subdomains of the thalamic nuclei (AV, AM, and Re), while the pyramidal layer of each innervates distinct cortical and subcortical targets.

(C) Simplified summary of the molecular markers and connectivity of the Sub and PS along the DV axis. Note the complementary gradient in size of the Sub and PS along the DV axis: the Sub dominates the dorsal portion, while the PS dominates the ventral portion of the hippocampus.

For specific changes in size and extent of the Sub and PS along the DVaxis, see Figures 3 and S4. See also Figures S5, S6, S7,S8, S9, and S10; Tables S2 and S3.

KEY RESOURCES TABLE

REAGENT or RESOURCE	SOURCE	IDENTIFIER
Antibodies		
Rabbit polyclonal anti-Parvalbumin	Swant Inc.	Cat#PV 25; RRID: AB_10000344
Mouse monoclonal anti-Neurofilament H (SMI-32)	Covance	Cat#SMI-32R-100; RRID: AB_509997
Bacterial and Virus Strains		
AAV2/1.hSynapsin.EGFP.WPRE.bGH	UPenn Vector Core	Addgene AAV1; 105539
AAV2/1.CAG.FLEX.EGFP.WPRE.bGH	UPenn Vector Core	Addgene AAV1; 51502
Chemicals, Peptides, and Recombinant Proteins		
Trimethoprim (TMP)	Sigma-Aldrich	T7883-5G
Tamoxifen (TAM)	Sigma-Aldrich	T5648-5G
Deposited Data		
Mouse subicular transcriptomic data	NeMO	nemo:dat-61rv7xg; https://assets.nemoarchive.org/dat-61rv7xg.
Experimental Models: Organisms/Strains		
Mouse: C57BL/6J	The Jackson Laboratory	JAX:000664
Mouse: B6;129S-*Calb1*$^{tm2.1(cre)Hze}$/J, Calb1-IRES2-Cre	The Jackson Laboratory	JAX:028532
Mouse: B6(Cg)-*Cux2*$^{tm1.1(cre)Mull}$/Mmmh, Cux2-IRES-Cre	MMRRC	MMRRC: 031778
Mouse: STOCK Tg(Dlg3-cre)KG118Gsat/Mmucd, Dlg3-Cre_KG118	MMRRC	MMRRC: 032809
Mouse: Drd1a-Cre	Richard Palmiter	N/A
Mouse: STOCK Tg(Drd3-cre)KI196Gsat, Drd3-Cre_KI196	MMRRC	MMRRC: 034610
Mouse: STOCK Tg(Drd3-cre)KI198Gsat/Mmucd, Drd3-Cre_KI198	MMRRC	MMRRC: 031741
Mouse: B6(Cg)-*Etv1*$^{tm1-1(cre/ERT2)Zjh}$/J, Etv1-CreERT2	The Jackson Laboratory	JAX: 013048
Mouse: STOCK *Gad2*$^{tm2(cre)Zjh}$/J, Gad2-IRES-Cre	The Jackson Laboratory	JAX: 010802
Mouse: STOCK Tg(Gal-cre)KI87Gsat/Mmcd, Gal-Cre_KI87	MMRRC	MMRRC: 031060
Mouse: STOCK Tg(Gpr26-cre)KO250Gsat/Mmucd, Gpr26-Cre_KO250	MMRRC	MMRRC: 033032
Mouse: C57BL/6-Tg(Grik4-cre)G32-4Stl/J, Grik4-Cre	The Jackson Laboratory	JAX:006474
Mouse: STOCK Tg(Grm2-cre)MR90Gsat/Mmcd, Grm2-Cre_MR90	MMRRC	MMRRC: 034611
Mouse: STOCK Tg(Grp-cre)KH288Gsat/Mmucd, Grp-Cre_KH288	MMRRC	MMRRC: 031183
Mouse: B6;129S-*Htr1a*$^{tm1.1(cre)Hze}$/J, Htr1a-IRES2-Cre	The Jackson Laboratory	JAX: 030160
Mouse: STOCK Tg(Kcnc2-Cre)K128Stl/LetJ, Kcnc2-Cre	The Jackson Laboratory	JAX:008582
Mouse: B6.Cg-*Ntng2*$^{tm1.1(cre)Hze}$/J, Ntng2-IRES2-Cre	The Jackson Laboratory	JAX:029588
Mouse: Otof-Cre	MMRRC	MMRRC: 032781
Mouse: Pcdh9-Cre_NP276	MMRRC	MMRRC: 036084
Mouse: STOCKTg(Plxnd1-cre)OG1Gsat/Mmucd, Plxnd1-Cre_OG1	MMRRC	MMRRC: 036631
Mouse: STOCK Tg(Ppp1r17-cre)NL146Gsat/Mmucd, Ppp1r17-Cre_NL146	MMRRC	MMRRC: 036205
Mouse: STOCK Tg(Rbp4-cre)KL100Gsat/Mmucd, Rbp4-Cre_KL100	MMRRC	MMRRC: 031125
Mouse: B6;129S-*Rorb*$^{tm1.1(cre)Hze}$/J, Rorb-IRES2-Cre	The Jackson Laboratory	JAX:023526
Mouse: B6;C3-Tg(Scnn1a-cre)3Aibs/J, Scnn1a-Tg3-Cre	The Jackson Laboratory	JAX:009613

REAGENT or RESOURCE	SOURCE	IDENTIFIER
Mouse: STOCK Tg(Sim1-cre)KJ18Gsat/Mmucd, Sim1-Cre_KJ18	MMRRC	MMRRC: 031742
REAGENT or RESOURCE	SOURCE	IDENTIFIER
Mouse: STOCK *Slc17a6*$^{tm2(cre)Lowl}$/J, Slc17a6-IRES-Cre	The Jackson Laboratory	JAX: 016963
Mouse: B6;129S-*Slc17a7*$^{tm1.1(cre)Hze}$/J, Slc17a7-IRES2-Cre	The Jackson Laboratory	JAX: 023527
Mouse: STOCKTg(Syt17-cre)NO14Gsat/Mmucd, Syt17-Cre_NO14	MMRRC	MMRRC: 034355
Mouse: B6;Cg-*Trib2*$^{tm1.1(cre/ERT2)Hze}$/J, Trib2-F2A-CreERT2	The Jackson Laboratory	JAX: 022865
Mouse: STOCK Tg(Vipr2-cre)KE2Gsat/Mmucd, Vipr2-Cre_KE2	MMRRC	MMRRC: 034281
Mouse: B6;129S-*Snap25*$^{tm2.1(cre)Hze}$/J Snap25-IRES2-Cre	The Jackson Laboratory	JAX: 023525
Mouse: *B6.Cg-Gt(ROSA)26Sor*$^{tm14(CAG-tdTomato)Hze}$/J, Ai14(RCL-tdT)	The Jackson Laboratory	JAX: 007914
Software and Algorithms		
DoubletFinder package	McGinnis et al., 2019	https://github.com/chrismcginnis-ucsf/DoubletFinder
Differential gene expression package	Ritchie et al., 2015	https://bioconductor.org/packages/release/bioc/html/limma.html
R package scrattch.hicat	Allen Institute	https://github.com/AllenInstitute/scrattch.hicat
Other		
Allen Mouse Brain CCF (v3)	Wang et al., 2020	http://atlas.brain-map.org/
Allen Mouse Brain Atlas	Lein et al., 2007	http://mouse.brain-map.org
Allen Mouse Brain Connectivity Atlas	Oh etal., 2014	http://connectivity.brain-map.org